# Graphical Abstract

## Probabilistic Quantification of Tsunami Currents in Karachi Port, Makran Subduction Zone, using Statistical Emulation

Devaraj Gopinathan,Mohammad Heidarzadeh,Serge Guillas

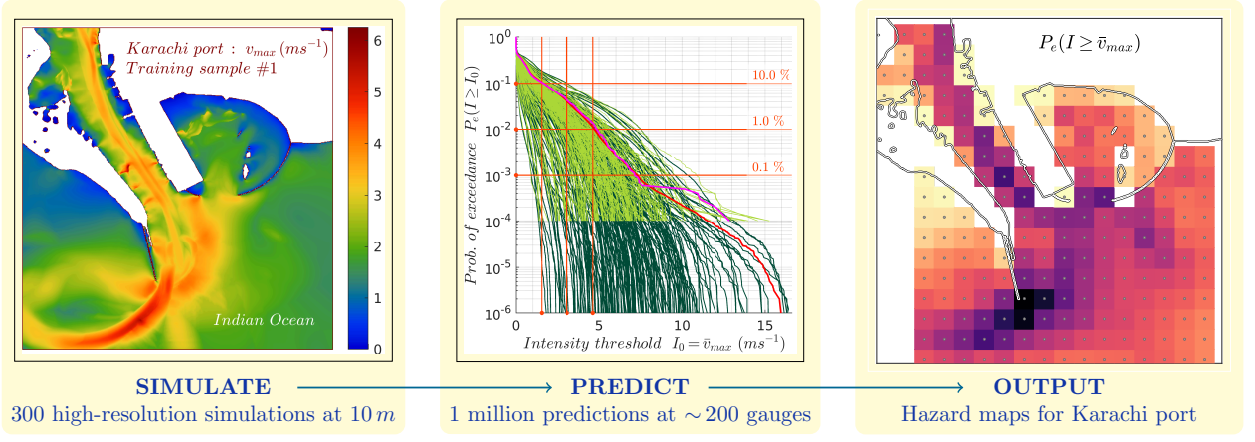

# Highlights

## Probabilistic Quantification of Tsunami Currents in Karachi Port, Makran Subduction Zone, using Statistical Emulation

Devaraj Gopinathan,Mohammad Heidarzadeh,Serge Guillas

- First hazard maps of port currents using 1 million scenarios (at 10 $m$ resolution)
- Greater than 50 % variation in velocities at harbor's mouth
- Maximum exceedance $\sim 18/10/4$ % for velocities $\sim 1.5/3/4.5\, ms^{-1}$ respectively
- Maximum velocities $\sim 3/7.5/10\, ms^{-1}$ for exceedance $10/1/0.1$ % respectively
- Up to 60 % seabed deformation amplification due to sediments

# Probabilistic Quantification of Tsunami Currents in Karachi Port, Makran Subduction Zone, using Statistical Emulation

Devaraj Gopinathan[a,*], Mohammad Heidarzadeh[b] and Serge Guillas[a]

[a]*Department of Statistical Science. University College London, Gower Street, London WC1E 6BT, UK.*
[b]*Department of Civil & Environmental Engineering. Brunel University London, Uxbridge UB8 3PH, UK.*

ARTICLE INFO

*Keywords*:
tsunami currents
port currents
statistical emulation
probabilistic hazard assessment
Karachi port
Makran subduction zone

ABSTRACT

In this paper, we model the full range of possible local impacts of future tsunamis in the Makran subduction zone (MSZ) at Karachi port, Pakistan. For the first time, the 3-D subduction geometry Slab2 is employed in the MSZ, in conjunction with the most refined rupture segmentation to date for this region, to improve the earthquake source definition. Motivated by the massive sediment layer over the MSZ, we also introduce to tsunami modeling the application of the sediment amplification formula, resulting in enhancements of seabed deformation up to 60 % locally. Furthermore, we design a new unstructured mesh algorithm for our GPU-accelerated tsunami code in order to efficiently represent flow velocities, including vortices, down to a resolution of 10 $m$ in the vicinity of the port. To afford to compute very large number of high resolution tsunami scenarios, for the granularity and extent of the range of magnitudes (occurrence ratios of $1 : 100,000$ implied by the Gutenberg-Richter relation) and locations of source, we create a statistical surrogate (*i.e.* emulator) of the tsunami model. Our main contribution is hence the largest set of emulated predictions using any realistic tsunami code to date: 1 million per location. We go on to obtain probabilistic representations of maximum tsunami velocities and heights at around 200 locations in the port area of Karachi. Amongst other findings, we discover substantial local variations of currents and heights. Hence we argue that an end-to-end synthesis of advanced physical, numerical and statistical modeling is instrumental in coastal engineering to comprehensively model local impacts of tsunamis.

## 1. Introduction

Destructive tsunami currents in ports have attracted the attention of coastal engineering community in recent years (Park and Cox, 2016). Following the unexpected damage incurred at ports from the tsunamis of 2004 (Indian Ocean), 2010 (Chile) and 2011 (Japan) (Borrero et al., 2015b; Okal et al., 2006), it is of paramount importance to investigate the associated hazard. Ports are vital economic lifelines and thus need to be safeguarded from natural disasters to prevent *e.g.* a sudden interruption of trade and commerce, a halt in the flow of essential commodities, as well as the destruction of livelihoods of fishermen communities. Despite recent studies (Borrero et al., 2015a,b; Lynett et al., 2012, 2014) and advances in high-fidelity modeling (Lynett et al., 2017), probabilistic methods tackling the quantification of future tsunami hazard due to strong flows in harbors are sparse (Park and Cox, 2016; Gonzalez et al., 2013). The need for such probabilistic quantifications is further accentuated by certain peculiarities that were observed with the phenomena of tsunami currents in ports. On 26 December 2004, the Sumatra-Andaman (SA) tsunami waves at the Omani port of Salalah wrested the freighter *Maersk Mandraki* from the main wharf before it was shoved around by the

*Corresponding author
d.gopinathan@ucl.ac.uk (D. Gopinathan); mohammad.heidarzadeh@brunel.ac.uk (M. Heidarzadeh); s.guillas@ucl.ac.uk (S. Guillas)
ORCID(s): 0000-0002-0490-3229 (D. Gopinathan); 0000-0002-1112-1276 (M. Heidarzadeh); 0000-0002-3910-3408 (S. Guillas)

vortices induced from the tsunami currents (Okal et al., 2006). The 285 $m$ long ship drifted uncontrollably for hours, despite manual intervention (Figure 1). It looped both inside and outside the harbor prior to winding up on a sand bar. Another anomaly was observed on 24 September 2013, when a submarine landslide in the Makran subduction zone (MSZ) generated a tsunami in the North-Western (NW) Indian Ocean, affecting the coasts of Oman, Iran, Pakistan and India (Heidarzadeh and Satake, 2014). The landslide that caused the tsunami was the secondary effect of a small $M_w$ 7.7 inland strike-slip earthquake. Tide-gauge records displayed tsunami waves of small amplitude ($20 \pm 7\ cm$) in the affected regions, except for three Omani ports (Heidarzadeh and Satake, 2014, Table 1 & Figure 3). Relatively larger amplitudes were found in the ports of Muscat (51 $cm$), Quarayat (109 $cm$) and Sur (40 $cm$). Here, the waves also prevailed for a relatively longer duration ($\gtrapprox 6\ h$) compared to the other ports (Figure 1).

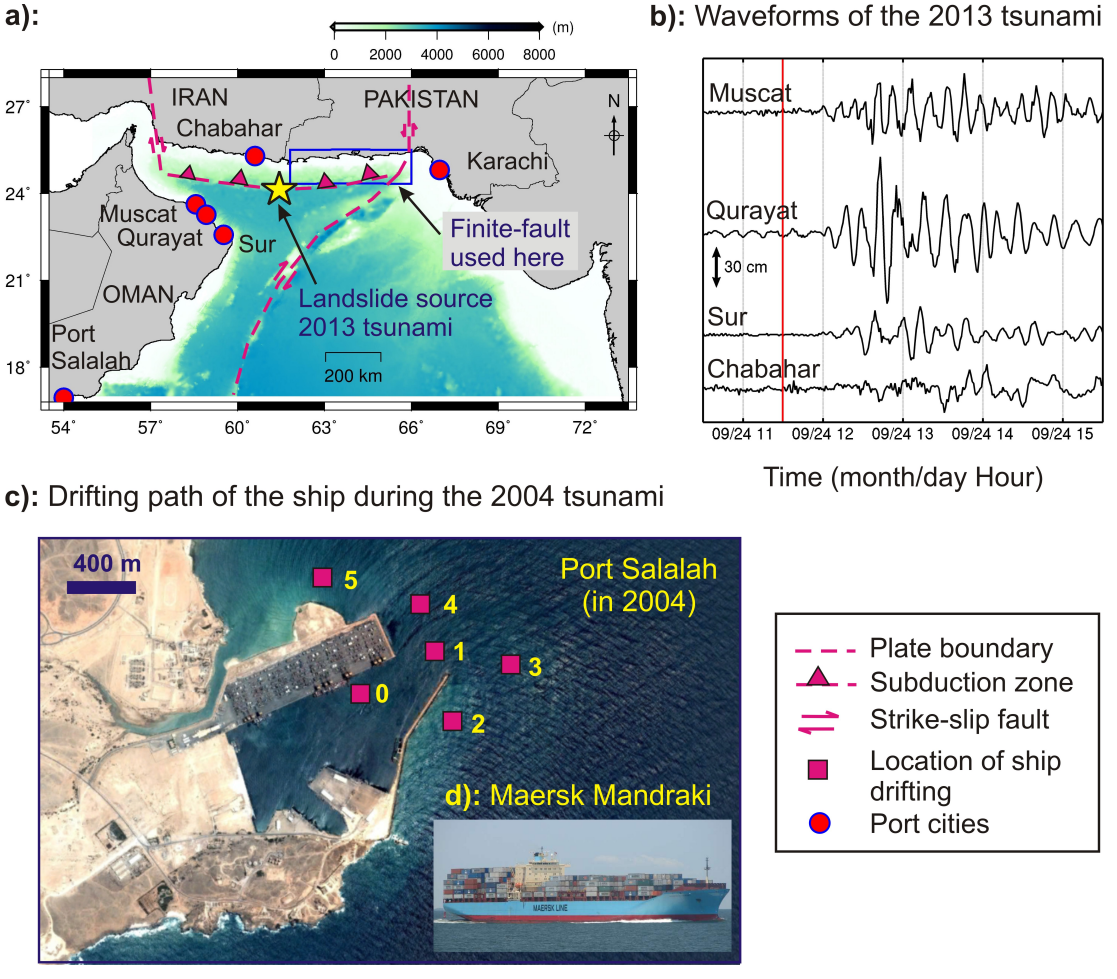


**Figure 1:** a) The Makran subduction zone area showing Karachi port studied in this work. b) Waveforms of the tsunami generated by a submarine landslide in the Makran region on 24 September 2013 based on Heidarzadeh and Satake (2014, Figure 11). c) Drifting of a large ship, the *Mearsk Mandraki* (shown in panel d) within the port of Salalah (pink squares) following the December 2004 Indian Ocean tsunami based on the data by Okal et al. (2006). The numbers to the right of each point indicate the sequence in which the ship drifted. d) The ship *Mearsk Mandraki* which was drifting in port Salalah following the 2004 Indian Ocean tsunami.

Overall, the above case from the 2004 tsunami provides evidence of the treacherous nature of tsunami currents in harbors. Although it may seem rational to associate high wave amplitudes with high velocities, the arresting feature is that the strong currents continued for hours after the waves with maximum amplitude had arrived (nearly 9 $h$ in Salalah). This is all the more consequential since conventional tsunami warnings may be lifted after visibly perceptible signs of the tsunami (*i.e.* vertical displacement) have disappeared, whereas the strong currents may manifest later on. In the case of the 2013 Makran tsunami also, it is highly probable that the coastal geometry and local bathymetry were responsible for long tsunami oscillations.

The Makran Subduction Zone (MSZ) has given rise to tsunamis in 1945 (Byrne et al., 1992; Heidarzadeh et al., 2008) and 2013 (Heidarzadeh and Satake, 2014). Recent studies estimate the megathrust potential for the eastern part of the MSZ (blue rectangle, Figure 1) to be $M_w$ 8.8 – 9.0 (Smith et al., 2013). Given the peculiarities observed in Makran ports during the 2004 and 2013 tsunamis, there is a pressing need for a comprehensive quantification of tsunami hazard, and associated uncertainties, especially port velocities. However, the accurate simulation of tsunami currents at shallow depths requires accurate coastline definition, high resolution bathymetry, and highly refined meshes, over enough time to capture the maximum. Thus, in this study we employ spatial resolutions of 10 $m$ for coastline, 30 $m$ for bathymetry, and 10 $m$ for the computational mesh, locally in the vicinity of Karachi port (Pakistan), for a total simulation time of 12 hours. The large number of runs, at such resolutions, needed for probabilistic hazard assessments stretches the limit of current High-performance Computing facilities, even with the latest GPU (Graphics Processing Unit) acceleration (Reguly et al., 2018). In terms of the seabed deformation given as input to the tsunami model, we introduce here an earthquake source designed with segments of size 5 $km \times 5$ $km$ with carefully constructed positive slip kernels to preserve fidelity to both magnitude scaling (Blaser et al., 2010) and slip scaling relations (Allen and Hayes, 2017). Second, the presence of a considerable sediment layer over the Makran Subduction Zone (MSZ) (up to 2 $km$) demands incorporation of its influence on the deformation, since a remarkable amplification of up to 60 % can be generated (Dutykh and Dias, 2010).

We select a probabilistic route in order to quantify uncertainties in future tsunamis due to the uncertain earthquake source variations (see the full workflow in Figure 2). However, since the probability of large events is small, a comprehensive coverage of the Gutenberg-Richter relation requires a large number of runs for the diversity of plausible events to be well represented across magnitudes and source location (in the thousands at minimum for a coarse quantification and much more for realistic assessments). Due to the considerable computational complexity of each high-resolution tsunami simulation of coastal tsunami currents, such a probabilistic endeavor can only be achieved by replacing the numerical tsunami model by a statistical surrogate: the emulator. To our knowledge, this is the first time that emulation has been marshalled to generate future earthquake-generated tsunami currents; it has been employed only once in the past for currents, for a single source of landslide-generated tsunamis with huge benefits in terms of computational

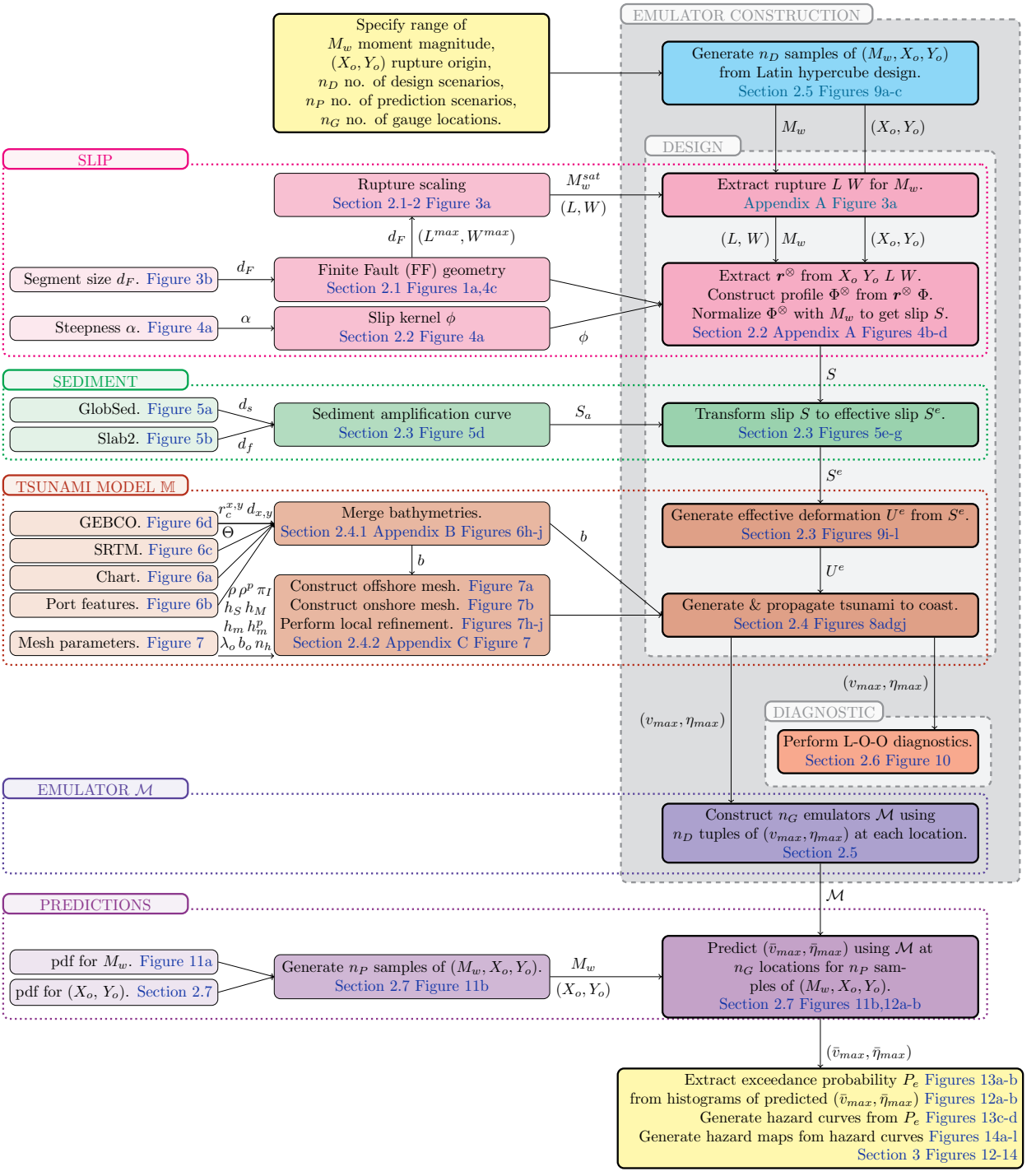


**Figure 2:** Global workflow describing the integration of different work components in this study for emulation-based probabilistic assessment of hazard for tsunami currents and heights in the port.

costs and hazard assessment (Salmanidou et al., 2019). With a design of only 300 runs, we fit an emulator to produce 1 million plausible tsunamis at any location. These emulated runs enable us to fully characterize uncertainty in future

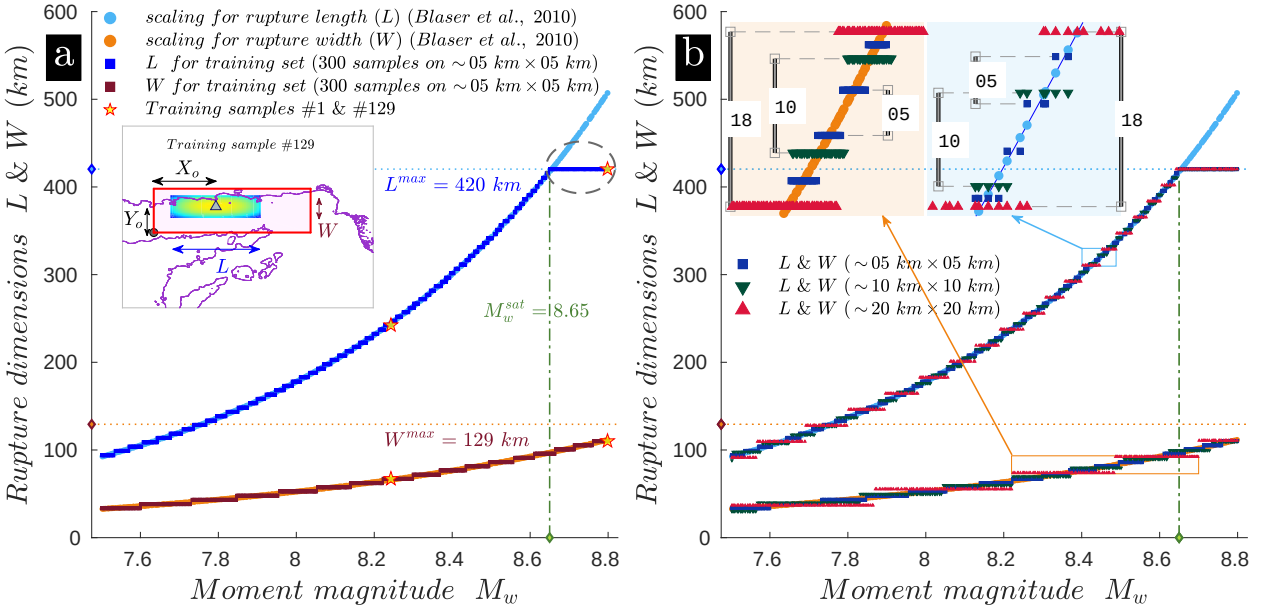


**Figure 3:** Finite fault model. a) Scaling relation of rupture length ($L$) and width ($W$) with respect to the rupture moment magnitude ($M_w$) showing the maximum length ($L_{max}$), width ($W_{max}$) and moment magnitude ($M_w^{sat}$) accommodable in the eastern MSZ. The lengths and widths of 300 earthquake scenarios are plotted over the scaling relation for an FF model made up of $\sim 5\,km \times 5\,km$ segments. The rupture length saturates after $M_w$ 8.65 (green line) in the region marked by the ellipse. The inset plot display the rupture dimensions $(L, W)$ and rupture origin co-ordinates $(X_o, Y_o)$ on a sample scenario (no. 129). Sample nos. 1 and 129 are marked on the scaling curves. b) Same as (a) but also includes FF models made up of $\sim 5\,km \times 5\,km$, $\sim 10\,km \times 10\,km$ and $\sim 20\,km \times 20\,km$ segments. The inset plots zoom on to the scaling relation to reveal discontinuities in the realizable fault dimensions.

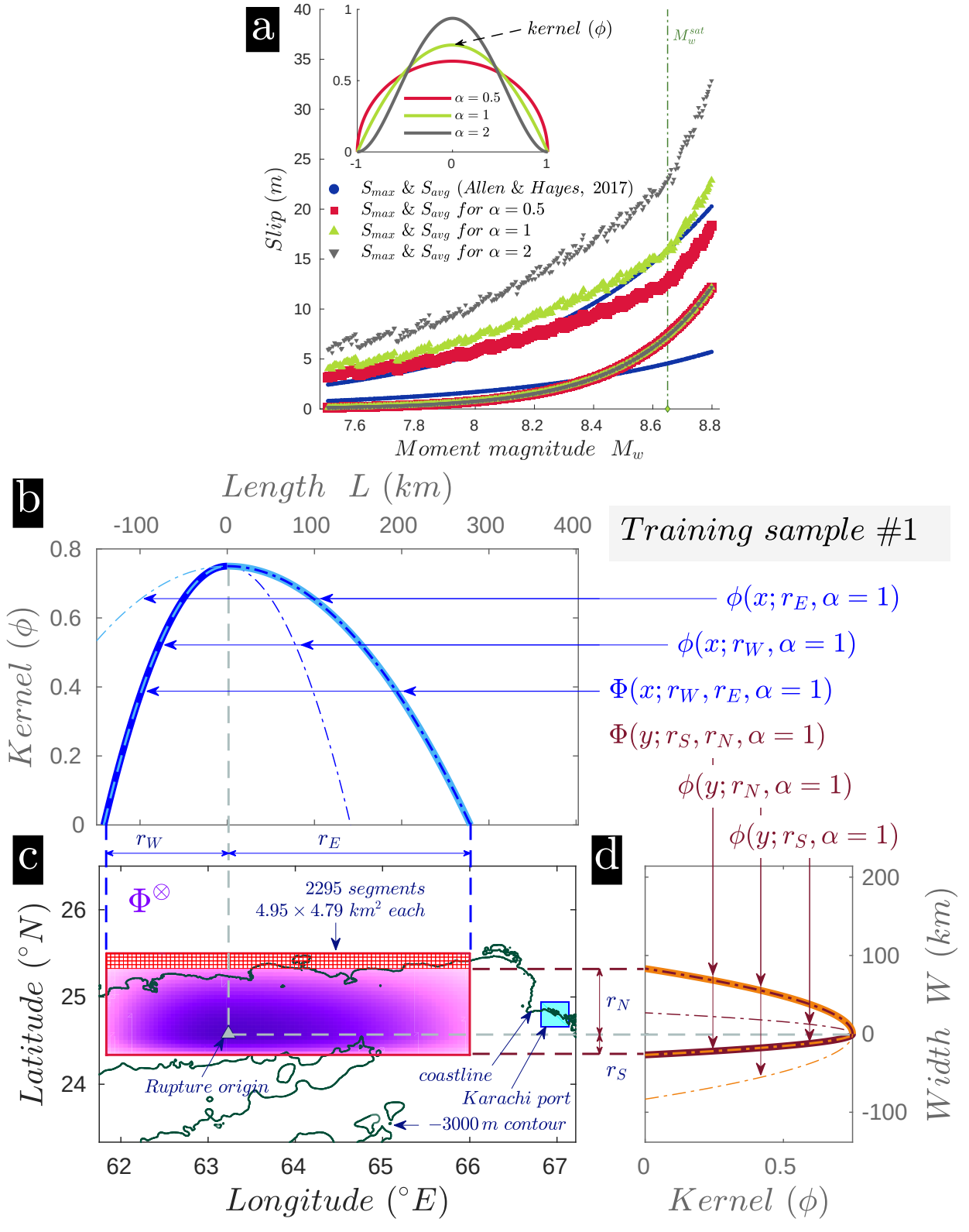


**Figure 4:** Slip profile generation. a) Validating maximum slips ($S_{max}$) and average slips ($S_{avg}$) for 300 earthquake scenarios as per the scaling relation in Allen and Hayes (2017) by varying the steepness ($\alpha$) b) & d) Bi-lobed kernels $\Phi\left(x; r_E, r_W, \alpha\right)$ and $\Phi\left(y; r_S, r_N, \alpha\right)$ along fault length and width respectively for a sample scenario (no. 1). c) Tensor product $\Phi^{\otimes}$ of the two bi-lobed kernel functions in (b) and (d) prior to magnitude normalization.

tsunami currents. Section 2 describes the models and methods used in this work, Section 3 discusses the results, and conclusions are drawn in Section 4.

## 2. Models, Data and Methods

In this section, we describe the finite fault apparatus (Section 2.1), construction of the slip profile on the finite fault (Section 2.2), integration of the sediment amplification over the slips (Section 2.3), tsunami propagation (Section 2.4), merging of bathymetries at different resolutions (Section 2.4.1), design of algorithm for locally refined unstructured mesh (Section 2.4.2), emulator training (Section 2.5), emulator diagnostics (Section 2.6) and finally the hazard predictions for 1 million events (Section 2.7). The global workflow is displayed in Figure 2.

There are formidable computational challenges that must be addressed in order to accurately represent both the actual geophysical processes and their uncertainties. Often, in tsunami modeling this trade-off between capability and capacity in High Performance Computing (HPC) is left unresolved by either radically simplifying the physics (*e.g.* a linear tsunami propagation till say $100\,m$ depth with the use of an empirical relationship thereafter), or running only a few high resolution simulations as scenarios. We argue that our tsunami emulation framework, in this context of currents that are highly nonlinear and very sensitive to near shore bathymetry, provides a solution to this trade-off between precision and coverage of uncertainties. It requires manipulation of very large data sets on HPC, as well as complex post-processing on diverse software and data platforms. Thus, our work here is at the forefront of what can be achieved using the most refined finite fault segmentation, the latest tsunami model acceleration schemes on GPU clusters, hierarchical file formats, smart unstructured meshes and newest multi-threading emulation platforms.

### 2.1. Finite Fault Model

We construct a finite fault (FF) on the eastern section of MSZ (blue rectangle, Figure 1) using a total number $\left(n_F\right)$ of 2295 rectangular segments (Figures 4c & 9j). The overall dimension of the FF model is $420\,km \times 129\,km$ ($L^{max} \times W^{max}$). The slip on a segment is denoted by $S_i$, where $i$ varies from 1 to 2295. The closed-form equations from Okada (1985) transform the slips and other FF parameters into a static vertical displacement denoted by $U$ (calculated inside an uplift calculation box, see Figures 9g & h). The final vertical displacement field results from the combined superposition of vertical displacements due to all the activated fault segments. Among the FF parameters, the dip angle and fault depth ($d_f$) are sourced from the recent plate boundary model, Slab2 (Hayes et al., 2018; Hayes, 2018). The strike and rake angles are kept constant at 270° and 90°. Each segment size ($d_F$) is approximately $5\,km \times 5\,km$ ($l_i \times w_i$). All the segments are arrayed in an $85 \times 27$ grid. This resolution is chosen to preserve fidelity to the scaling relation from Blaser et al. (2010) (Figure 3a), arrived through comparing the performance of different segment sizes *viz.* $5\,km \times 5\,km$, $10\,km \times 10\,km$ and $20\,km \times 20\,km$ (Figure 3b). The discrepancy to the scaling relation appears as

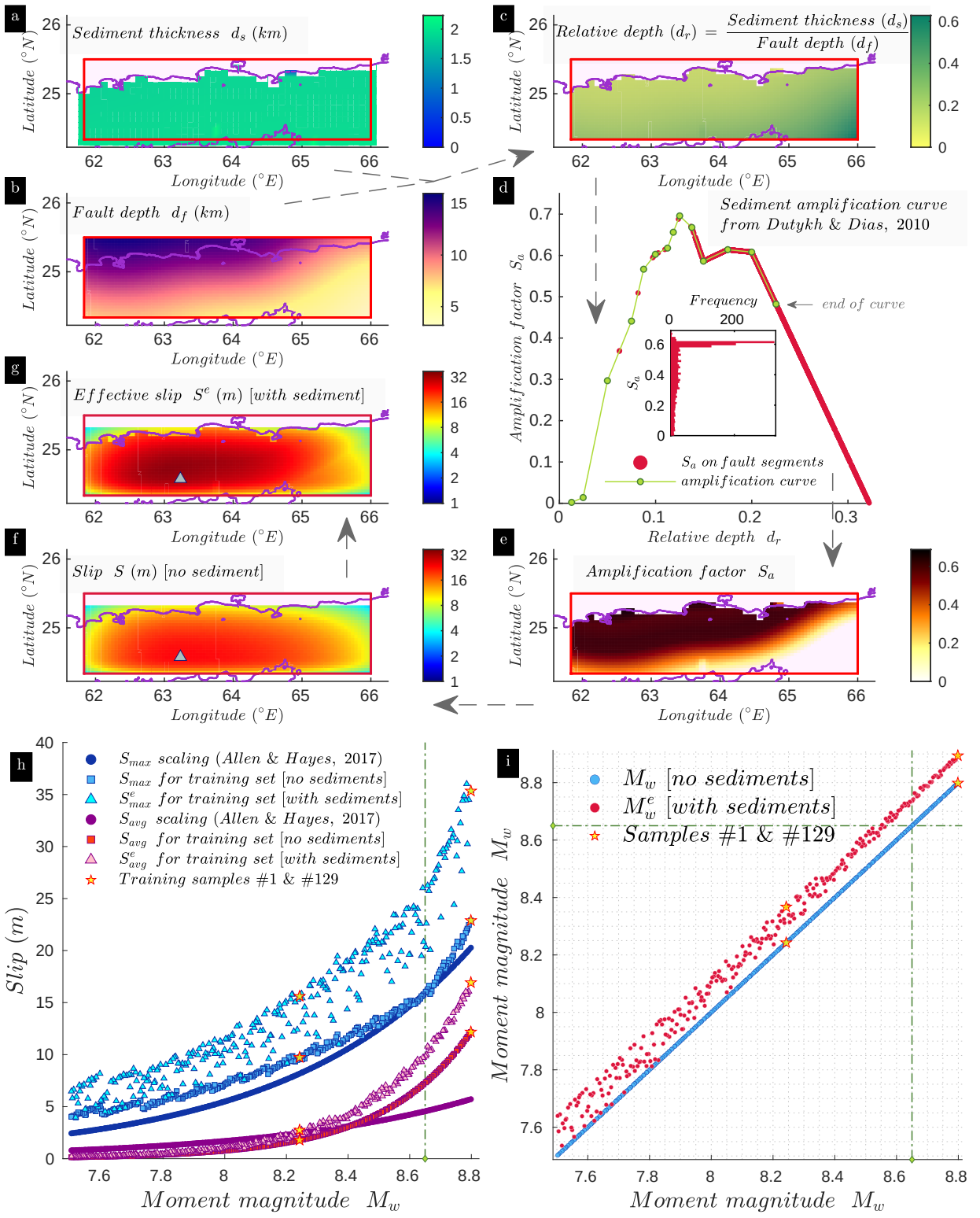


**Figure 5:** Sediment amplification. a) Sediment thickness $d_s$ over eastern MSZ. b) Fault depth $d_f$. c) Relative depth $d_r$. d) Sediment amplification curve from Dutykh and Dias (2010). The inset histogram shows the distribution of $S_a$ for all the FF segments. e) Sediment amplification factor $S_a$. f) Slip profile $S$ without sediments. g) Effective slip profile $S^e$ incorporating influence of sediments. h) Comparison of $S_{avg}$ and $S_{max}$ with and without the influence of sediments to slip scaling in Allen and Hayes (2017). i) Same as (h) but for moment magnitude with ($M^e_w$) and without ($M_w$) the effect of sediments.

discontinuities in the realizable fault lengths ($L$) and widths ($W$) (Figure 3a inset). The size of the discontinuities are the same as the resolution chosen (Figure 3b inset). Thus, we observe the least discontinuity while using a $5\,km \times 5\,km$ segmentation (Figure 3). We use the definitions of the seismic moment $M_w$ and moment magnitude $M_0$ (Kanamori, 1977; Hanks and Kanamori, 1979) as,

$$M_w = (2/3)\left(\log_{10} M_0 - 9.1\right), \qquad M_0 = \sum_{i=1}^{n_F} \mu l_i w_i S_i \tag{1}$$

with $\mu = 3 \times 10^{10}\ N/m^2$ being the modulus of rigidity. Our implementation of the Okada suite is adapted from the dMODELS[1] code (Battaglia et al., 2012, 2013). The next section details the design of the slip profile over the FF model.

## 2.2. Slip Profile Generation

Slips are usually modeled to be uniform on the FF segments, even though inversions of seismic sources evidenced localised concentrations of high slips or asperities over a backdrop of lower slips (Grezio et al., 2017). To generate a similar behaviour in our slip profiles, we utilize a positive kernel function $\phi$ having a functional form (Figure 4a inset):

$$\phi(x; r, \alpha) = \begin{cases} c_\alpha \left(1 - \left|\frac{x}{r}\right|^2\right)^\alpha & |x| \le r \\ 0 & |x| > r \end{cases} \tag{2}$$

where $c_\alpha = \dfrac{\Gamma(2l+2)}{2^{2l+1}\Gamma(l+1)^2}$ is the normalizing constant made up of the gamma function ($\Gamma$), the length scale $r$ defines the domain where $\phi$ is non-zero and the parameter $\alpha$ adjusts the steepness of $\phi$. Using $\phi$ as the core, we construct the bi-lobed kernel function $\Phi$:

$$\Phi\left(x; r_l, r_r, \alpha\right) = \begin{cases} \phi\left(x; r_l, \alpha\right) & -r_l \le x \le 0 \\ \phi\left(x; r_r, \alpha\right) & 0 \le x \le r_r \end{cases} \tag{3}$$

where $r_l$ and $r_r$ are the length scales of the left and right lobes of $\Phi$, their values depending on the position of the rupture origin $(X_o, Y_o)$ with respect to the fault length ($L$) and width ($W$) (Figures 3a inset & 4b-d). The tensor product of the two bi-lobed kernel functions, one along the length (Figure 4b) and another along the width (Figure 4d) of the fault yields the surface $\Phi^{\otimes}$ (Figure 4c):

$$\Phi^{\otimes}\left(x, y; \boldsymbol{r}^{\otimes}, \alpha\right) = \Phi\left(x; r_W, r_E, \alpha\right) \otimes \Phi\left(y; r_S, r_N, \alpha\right) \quad (x, y) \in \left[-r_W, r_E\right] \times \left[-r_S, r_N\right] \tag{4}$$

[1] v1.0 available at *pubs.usgs.gov/tm/13/b1/*

where $\left[-r_W, r_E\right] \times \left[-r_S, r_N\right]$ denotes the domain of the rupture and $\boldsymbol{r}^{\otimes} = \left\{r_W, r_E, r_S, r_N\right\}$. A normalization of $\Phi^{\otimes}$ with the required moment magnitude on the rupture yields the final slip profile $S$ (Figure 5f and 9e & f). The algorithm for the above construction is detailed in Appendix A. Given the algorithm, we arrive at $\alpha = 1$ by varying $\alpha$ to closely match the maximum slip $S_{max}$ and average slip $S_{avg}$ curves generated from the scaling relations in Allen and Hayes (2017, Table 2) (Figure 4a). The next section describes the incorporation of the effect of seafloor sediment layer.

## 2.3. Sediment Amplification

Considerable amplification (up to 60 % locally) of crustal deformation due to the presence of layers of sediments on the seafloor was shown in Dutykh and Dias (2010, Figure 12). We introduce it here in tsunami modeling, by making use of the sediment amplification curve (Figure 5d). The curve uses the relative depth ($d_r^i$) of the $i$th segment (Figure 5c) calculated as:

$$d_r^i = \frac{d_s^i}{d_f^i} \tag{5}$$

where $d_s^i$ is the sediment thickness over the segment interpolated from GlobSed[2] (Straume et al., 2019), and $d_f^i$ is the down-dip fault depth of the segment taken from Slab2 (Hayes et al., 2018) (Figures 5a & b). Given $d_r^i$, the sediment amplification curve supplies the sediment amplification factor ($S_a^i$) on the segment (Figure 5e). The amplification due to the sediments is incorporated by multiplying the slip $S^i$ (Figure 5f) with the sediment amplification factor $S_a^i$ resulting in an effective slip $S_i^e$ (Figure 5g):

$$S_i^e = S_i \left(1 + S_a^i\right) \tag{6}$$

The closed-form equations from Okada (1985) transform the effective slips $S_i^e$ into the effective vertical displacement $U^e$ (Figures 9k & l). The influence of sediments not only increases the slips but also modifies the profile, as evident in the emergence of a double-lobed profile in the effective slip (Figure 5g). The effect is more conspicuous in the associated deformations (compare Figures 9g & k). The amplification factor ($S_a$) peaks at a relative depth of approximately 0.13 after which it decreases. Given the geometry of the fault and overlying sediment profile, a significant number of segments have an amplification factor between $0.4 - 0.6$ (or, equivalently a $40 - 60$ % amplification) (Figures 5d inset & e). Furthermore, the sediment amplification factor for the whole MSZ is shown in Figure 5e; its value is strongly dominated by the fault depth (Figure 5b) rather than the sediment thickness (Figure 5a) which is uniform around 2 $km$. The sediment amplification curve is defined only till a relative depth of 0.23 in Dutykh and Dias (2010). We linearly extrapolate the curve in order to be as conservative as possible in the region where it is not defined as

[2] available from *ngdc.noaa.gov/mgg/sedthick/*

well as to smoothly transition from regions of higher to lower fault depths. The counterparts of average slip $S_{avg}$ and maximum slip $S_{max}$ of $S$ (without sediments) are defined as average effective slip $S^e_{avg}$ and maximum effective slip $S^e_{max}$ of $S^e$ (with sediments). Similarly, effective moment magnitude $M^e_w$ is defined, by replacing $S_i$ with $S^e_i$ in Eqn. 1. The effect of sediments on slips is compared in Figure 5h. Here, the increased scatter of $S^e_{max}$ compared to $S^e_{avg}$ is due to the spatial distribution of $S_a$, which significantly amplifies $S^e_{max}$ depending on the rupture origin $(X_o, Y_o)$. Also, the increase in scatter of $S^e_{max}$ as $M_w$ decreases is due to the decrease in rupture dimensions that allow many earthquake scenarios to be situated in areas of lower $S_a$. This aspect is pronounced in a similar comparison of $M^e_w$ to $M_w$ in Figure 5i. The next section describes the propagation of the tsunami resulting from the deformations caused by the effective slips.

## 2.4. Tsunami Propagation

Unlike simulations for analysing wave heights which require a few hours of simulation time, capturing the velocities need a longer simulation time. Thus, each scenario is run for 12 $h$ of simulation time ($T_s$) to obtain the maximum tsunami velocity and wave height, and therefore is computationally expensive. It is not only imperative that the numerical algorithms in the computer code for tsunami simulations run efficiently at fine mesh resolutions needed to capture the currents (10 $m$), but also that the code is amenable to adequate parallelisation. Thus, to run 300 such scenarios, we employ VOLNA-OP2[3] that has been shown to run efficiently for unstructured meshes on parallel GPUs (Reguly et al., 2018). The number of scenarios (*i.e.* 300) is considerably higher than in existing studies (Rashidi et al., 2020; Hasan et al., 2017; Heidarzadeh and Kijko, 2011). Usual simulations employ the Green's functions approach to superpose the tsunami wave heights due to a multi-segment finite fault source. Here, we use the the Non-linear Shallow Water Equations (NSWEs) to model not only the propagation of the tsunami but also the run-up/down processs at the coast (Dias et al., 2014). The finite volume (FV) cell-centered method for tessellation of control volume is used in VOLNA. Thus, the barycentres of the cells are associated with the degrees of freedom. Dutykh et al. (2011) and Giles et al. (2020) may be referred for details of numerical implementation, validation against standard benchmarks and comprehensive error analysis. VOLNA models the tsunami life-cycle with:

$$\frac{\delta H}{\delta t} + \nabla\cdot(H\boldsymbol{v}) = 0 \tag{7}$$

$$\frac{\delta H\boldsymbol{v}}{\delta t} + \nabla\cdot\left(H\boldsymbol{v}\otimes\boldsymbol{v} + \frac{g}{2}H^2\mathbf{I}_2\right) = gH\nabla b \tag{8}$$

[3] v1.5 available at *github.com/reguly/volna*, with improvements to second order FV scheme and boundary conditions

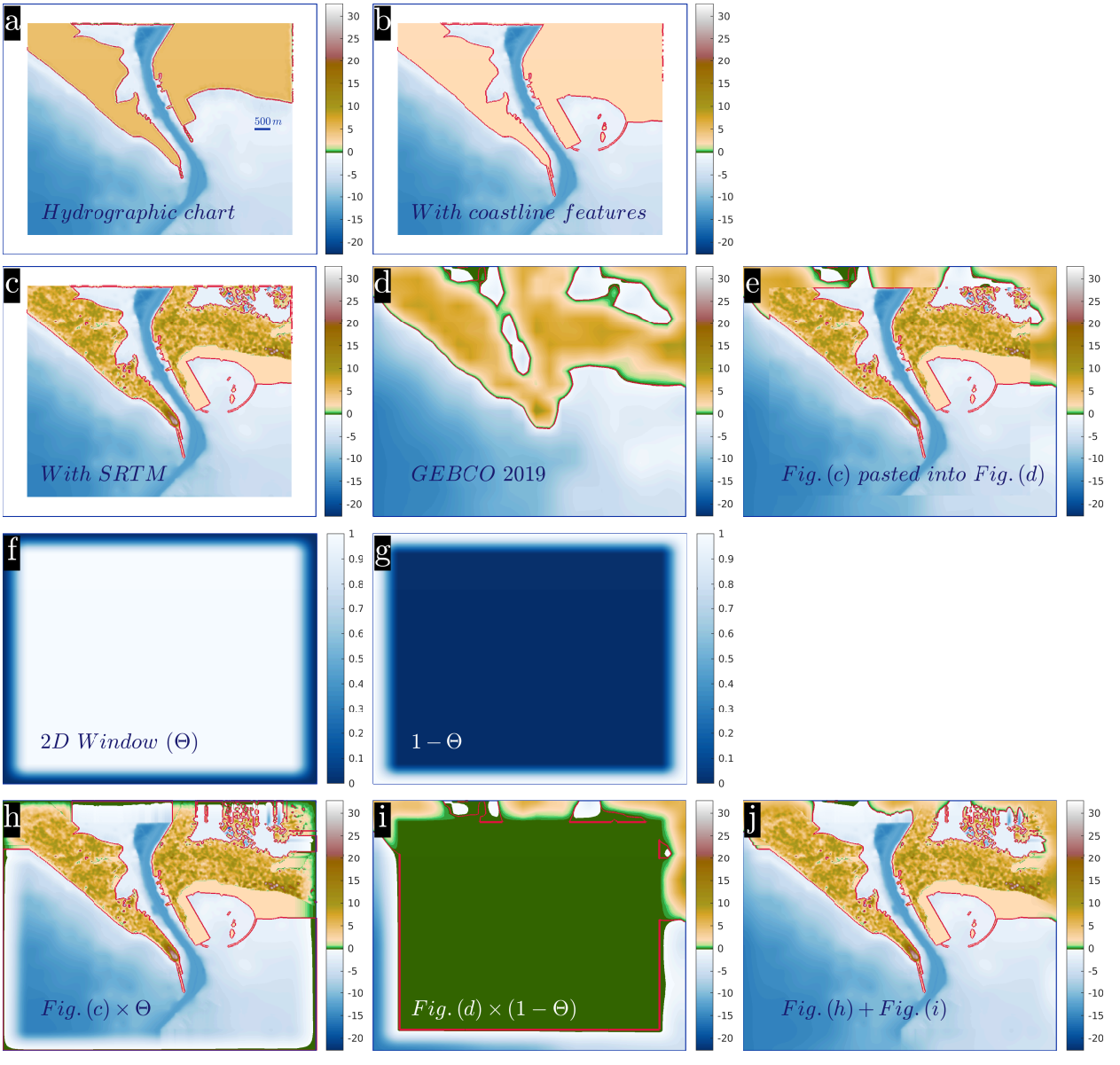


**Figure 6:** Merging of bathymetries. a) Digitized hydrographic chart bathymetry around Karachi port. b) Chart data with altered coastline after addition of port features from Google Earth. c) Chart data supplemented with SRTM data. d) GEBCO bathymetry around Karachi port. e) Merged bathymetry with chart data in (c) pasted into GEBCO bathymetry in (d). f) 2D window ($\Theta$). g) Complement of $\Theta$, *i.e.* $(1-\Theta)$. h) Chart bathymetry in (c) muliplied by window. i) GEBCO bathymetry in (d) multiplied by complement of window. j) Final merged bathymetry resulting from addition of windowed bathymetries in (h) and (i).

where $H(\boldsymbol{x},t) = b + \eta$ is the total water depth defined as the sum of free surface elevation $\eta(\boldsymbol{x},t)$, and time-dependent bathymetry $b(\boldsymbol{x},t)$. The two horizontal components of the depth-averaged fluid velocity are contained in $\boldsymbol{v}(\boldsymbol{x},t)$, $g$ is the standard gravity and $\mathbf{I}_2$ is the $2\times 2$ identity matrix. The maximum tsunami velocity $v_{max}$ and wave height $\eta_{max}$ at

a location $(\boldsymbol{x}, t)$ are computed as:

$$v_{max}(\boldsymbol{x}) = \max_{0 < t \leq T_s} \|\boldsymbol{v}(\boldsymbol{x}, t)\|_2 \tag{9}$$

$$\eta_{max}(\boldsymbol{x}) = \max_{0 < t \leq T_s} \eta(\boldsymbol{x}, t) \tag{10}$$

The dynamic bathymetry $b(\boldsymbol{x}, t)$ is composed as:

$$b(\boldsymbol{x}, t) = b_s(\boldsymbol{x}) + U^e(\boldsymbol{x}, t) \tag{11}$$

where $b_s$ is the static bathymetry and $U^e$ is the effective deformation due to the influence of sediments (Section 2.3). In this work, an instantaneous rupture is assumed, *i.e.* $U^e$ is supplied once at the beginning of the simulation. Further, to reduce the computational burden of calculating deformations from 300 ruptures, $U^e$ is computed only within a uplift calculation box covering the rupture (see green rectangle in Figures 9g-h & k-l). We now move on the bathymetry $b_s$ and unstructured mesh, both vital components for an accurate modeling of currents in shallow water and near the coast.

### *2.4.1. Merging of Bathymetries*

The bathymetry used for the simulations is sourced from the GEBCO 2019 data set (GEBCO Bathymetric Compilation Group 2019, 2019), having a resolution of $15''$ (Figure 6d). Accurate modeling of port velocities and currents near the coast requires high resolution bathymetry and good definition of the coastline. Towards this, we use digitized bathymetry data at a resolution of $\sim 30\,m$ from hydrographic charts for Karachi port (Figure 6a). Further, we correct the shoreline using satellite imagery from Google Earth at $\sim 10\,m$ resolution wherever port structures and breakwaters need to be resolved (Figure 6b). The charts do not contain topographic data, which we supplement with SRTM v3[4] $1''$ data (Figure 6c). Simply replacing the GEBCO data with the hydrographic chart data gives rise to sharp and unrealistic discontinuities in the merged data set (Figure 6e). We ameliorate this by smoothly merging the hydrographic data into the GEBCO data by a procedure using cosine-tapered Tukey windows (Figures 6f-g). The detailed algorithm can be found in Appendix B.

### *2.4.2. Localised Non-Uniform Unstructured Mesh*

We design a customised mesh algorithm for the unstructured mesh sizing function in three stages corresponding to offshore, onshore and port regions. A strategy based on bathymetry $b(\boldsymbol{x})$ is used to generate the mesh in sea (Figure 7a),

[4] available from *earthexplorer.usgs.gov*

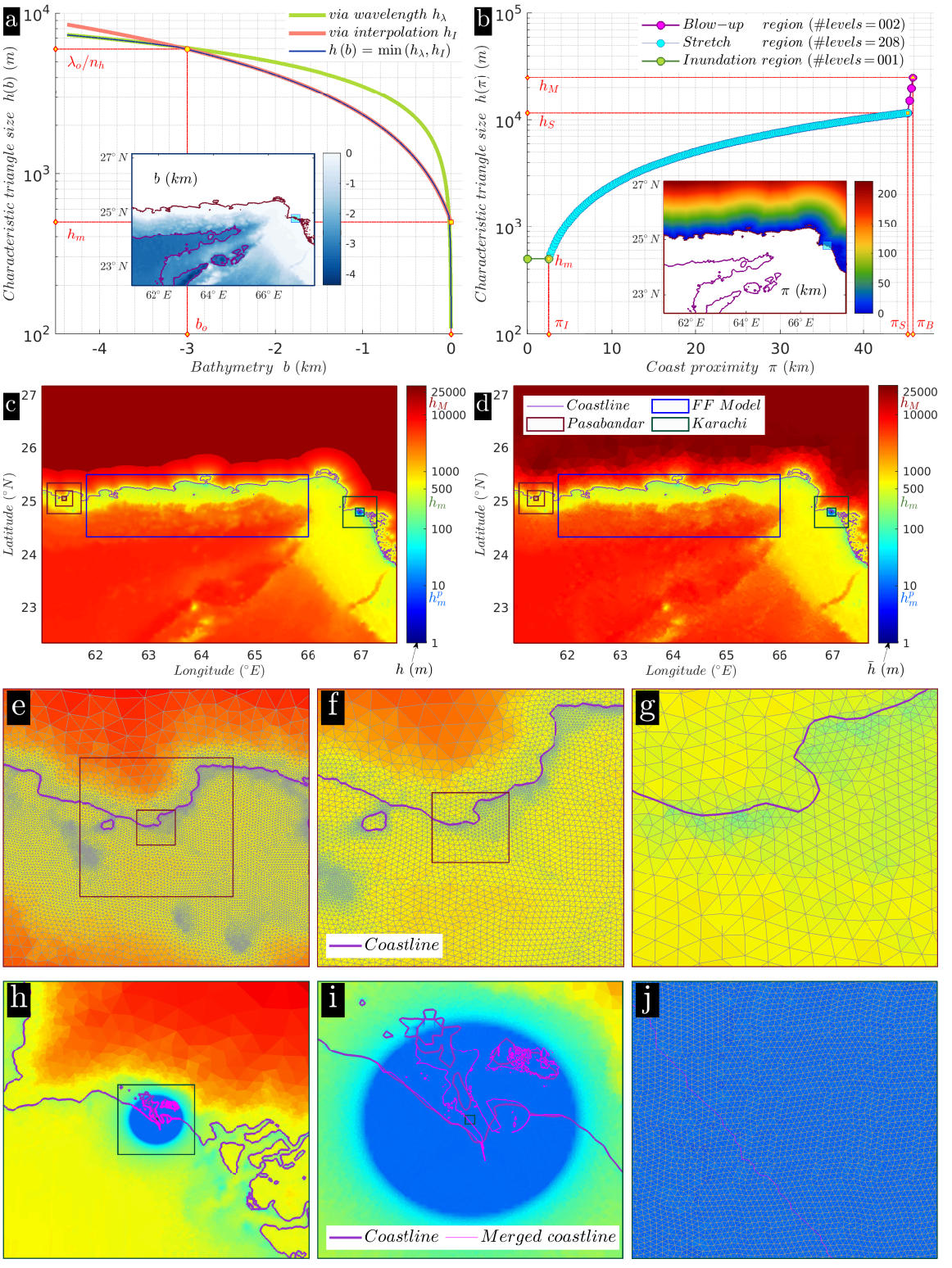


**Figure 7:** Localised non-uniform unstructured mesh. a) Mesh-sizing rule for offshore mesh based on bathymetry $b$, shown in the inset. b) Mesh-sizing rule for onshore mesh based on coast proximity $\pi$, shown in the inset. c) Mesh sizing function $h$ supplied to Gmsh for the whole domain resulting from the mesh-sizing rules in (a) and (b). d) Actual mesh sizes $\bar{h}$ in mesh generated from Gmsh using the mesh sizing function in (c). e-g) [*no local refinement*] Mesh at Pasabandar shown at scales of $64\,km \times 64\,km$, $32\,km \times 32\,km$ and $8\,km \times 8\,km$ respectively. h-j) [*with local refinement*] Mesh at Karachi port shown at scales of $64\,km \times 64\,km$, $16\,km \times 16\,km$ and $0.5\,km \times 0.5\,km$ respectively.

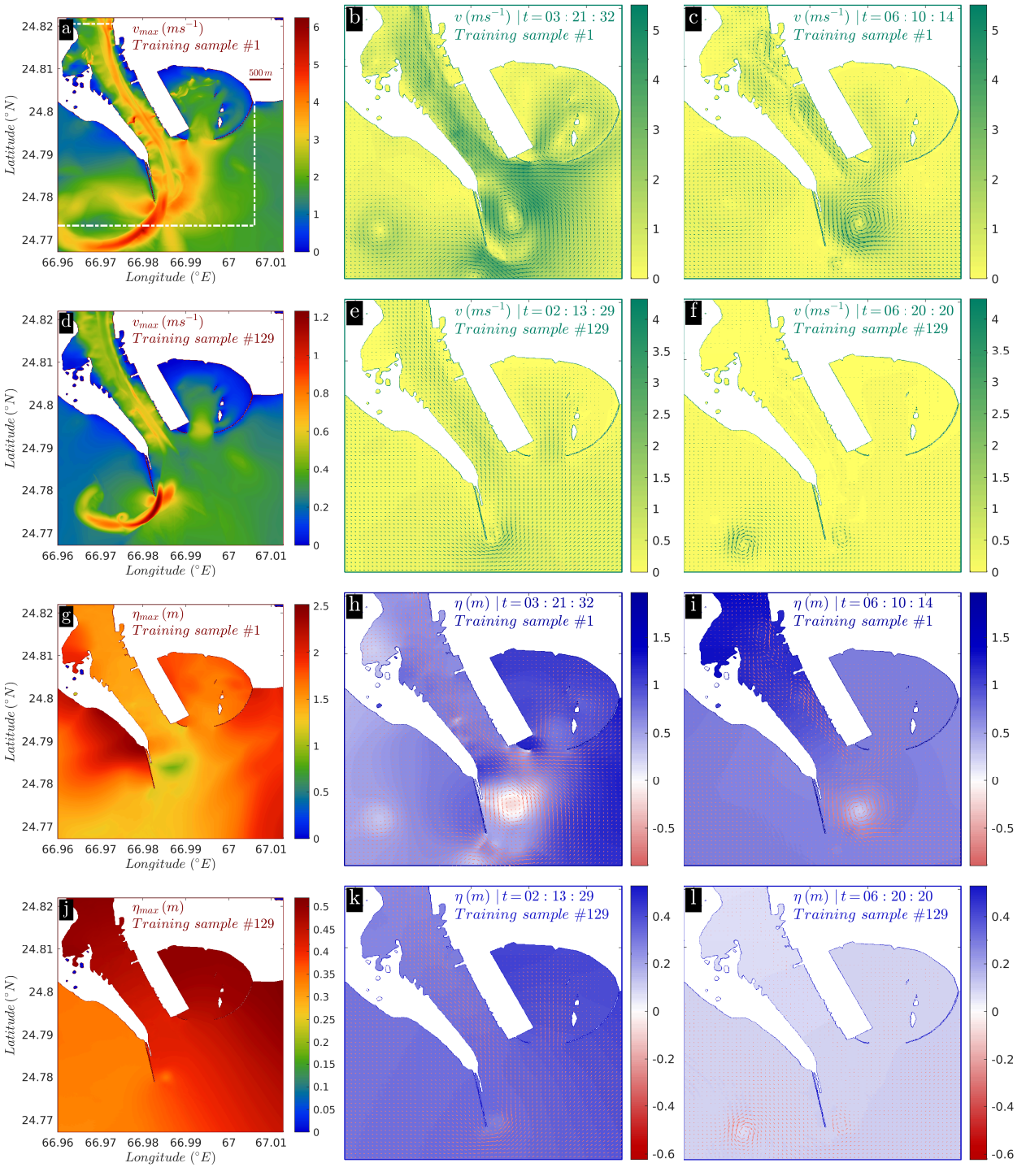


**Figure 8:** Tsunami propagation. a) Maximum velocity $v_{max}$ around Karachi port over a simulation time of $12\,h$ for sample no. 1. b-c) Snapshots of velocities $v$ for sample no. 1 at various times restricted to the box (dashed line) in (a). d-f) Same as (a-c) but for sample no. 129. g-l) Same as (a-f) but for tsunami height $\eta_{max}$ (and $\eta$).

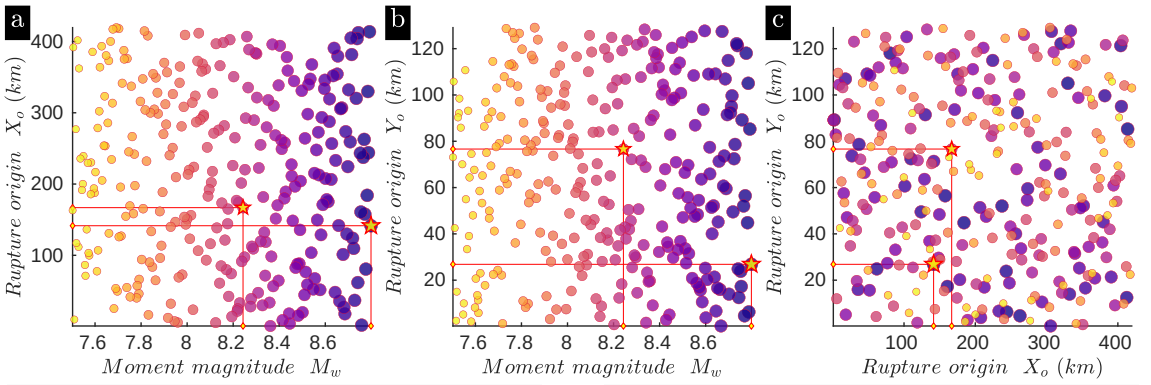


*Training sample #001*
*Rupture origin* $(X_o, Y_o) = (142, 027)$ *km*
*Rupture dimensions* $(L, W) = (420, 110)$ *km*

| | | | |
|---|---|---|---|
| $S_{avg}$ | 12.17 *m* | $S_{max}$ 22.88 *m* | $M_w$ 8.798 |
| $U_{min}$ | − 03.73 *m* | $U_{max}$ 05.63 *m* | *no sediments* |
| $S^e_{avg}$ | 16.92 *m* | $S^e_{max}$ 35.34 *m* | $M^e_w$ 8.894 |
| $U^e_{min}$ | − 05.80 *m* | $U^e_{max}$ 07.68 *m* | *with sediments* |

d

*Training sample #129*
*Rupture origin* $(X_o, Y_o) = (167, 077)$ *km*
*Rupture dimensions* $(L, W) = (242, 067)$ *km*

| | | | |
|---|---|---|---|
| $S_{avg}$ | 01.79 *m* | $S_{max}$ 09.73 *m* | $M_w$ 8.243 |
| $U_{min}$ | − 02.06 *m* | $U_{max}$ 02.30 *m* | |
| $S^e_{avg}$ | 02.75 *m* | $S^e_{max}$ 15.61 *m* | $M^e_w$ 8.367 |
| $U^e_{min}$ | − 03.24 *m* | $U^e_{max}$ 03.68 *m* | |

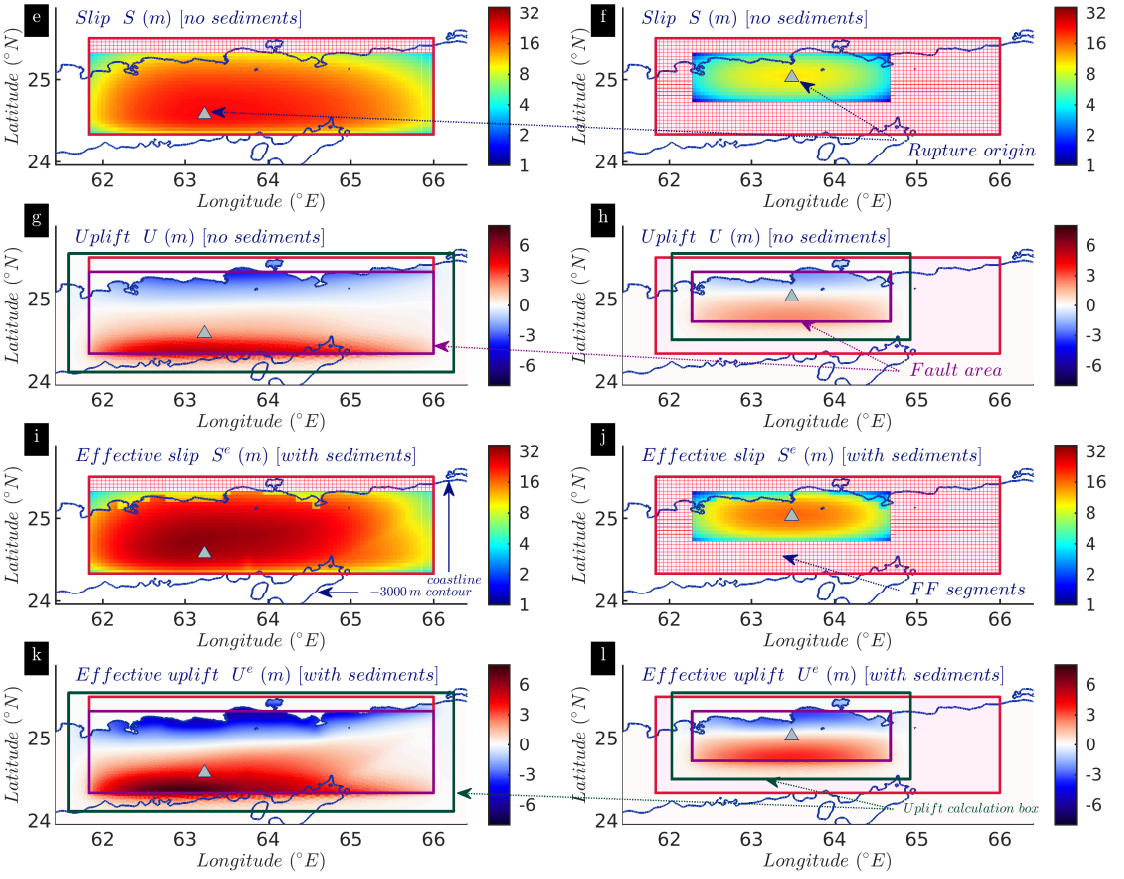


**Figure 9:** Training set of 300 scenarios of $(M_w, X_o, Y_o)$ generated by Latin Hypercube Design. a) Training set projected on $M_w - X_o$ plane. Sample nos. 1 and 129 are marked with stars. b) Same as (a) but on $M_w - Y_o$ plane. c) Same as (a) but on $X_o - Y_o$ plane. d) Comparison of relevant quantities for sample nos. 1 and 129. e) Slip $S$ for sample no. 1 before incorporation of sediment influence, plotted on $log_2$ scale. f) Same as (e) but for sample no. 129. g) Offshore deformation $U$ due to slip $S$ for sample no. 1. h) Same as (g) but for sample no. 129. i) Effective slip $S^e$ for sample no. 1 after incorporation of sediment influence. j) Same as (i) but for sample no. 129. k) Effective deformation $U^e$ due to slip $S^e$ for sample no. 1. l) Same as (k) but for sample no. 129.

whilst proximity to the coast $\pi(\boldsymbol{x})$ is used to size the mesh on land (Figure 7b). We also locally refine the mesh to $10\,m$ resolution at Karachi port (Figure 7h-j). This three pronged strategy strikes a balance between the fine mesh resolution required near the port for resolution of velocities and associated overall computational cost. The non-uniform meshes for the simulation are generated using Gmsh[5] (Geuzaine and Remacle, 2009). Considering the dimensions of the finite fault earthquake sources ($L \times W$), we assume an approximate source wavelength ($\lambda_o < \sqrt{L^2 + W^2}$) of the tsunami, and a representative ocean depth of the Makran trench ($b_o \sim 3\,km$), and calculate the time period ($T_\lambda$) of the wave as,

$$T_\lambda = \lambda_o / \sqrt{g b_o} \tag{12}$$

Here, $\lambda_o = 60\,km$, which is around 60 % of the maximum distance contained in the smallest rupture considered in this work, *i.e.* of size $\sim 94\,km \times 34\,km$ for a $M_w$ 7.5 event (sample no. 300). Next, assuming that the time period of the tsunami is the same everywhere in the domain, we get for a depth $b(\boldsymbol{x})$ (van Scheltinga et al., 2012),

$$\lambda_n / \sqrt{b(\boldsymbol{x})} = \lambda_o / \sqrt{b_o} \tag{13}$$

which in turn relates the characteristic triangle (or element) length $h_\lambda(b)$ for depth $b(\boldsymbol{x})$ as,

$$h_\lambda(b) = \left(\lambda_o / n_h\right) \sqrt{b(\boldsymbol{x}) / b_o} \tag{14}$$

where $n_h = \lambda_n / h_\lambda(b) = 10$ is the number of triangles in one wavelength $\lambda_n$. At the shore (*i.e.* $b = 0$), a minimum mesh size $h_m$ of $500\,m$ is specified. In the vicinity of the port, the mesh size $h_m^p$ is fixed as $10\,m$. We also fix the maximum triangle size ($h_M$) as $25\,km$ for regions that are deep inland. Further details and construction process for onshore and port mesh sizing functions are elaborated in Appendix C. After feeding the mesh sizing function (Figure 7c) into Gmsh, we get the computational mesh with ∼2.64 million cells or triangles (Figure 7d). Figures 7e-g & h-j show enlarged pictures of the mesh at increasingly fine scales for regions with (Pasabandar port) and without (Karachi port) local refinement respectively.

The outputs $v_{max}$ and $\eta_{max}$ for two training samples, no. 1 and 129 are plotted in Figure 8. The figures also contains snapshots taken at various time instants during the simulation.

## 2.5. Emulator Construction

The numerical simulation of the tsunami life cycle, *i.e.* its generation, propagation and inundation at fine mesh resolutions is computationally expensive due to non-linearity, and typically consumes hours on supercomputers. This is all the more prohibitive for a probabilistic quantification since thousands of runs of the forward model are required to adequately capture the various plausible scenarios. Statistical surrogates (or emulators) provide a computationally

[5] v4.4.1 available at *gmsh.info*

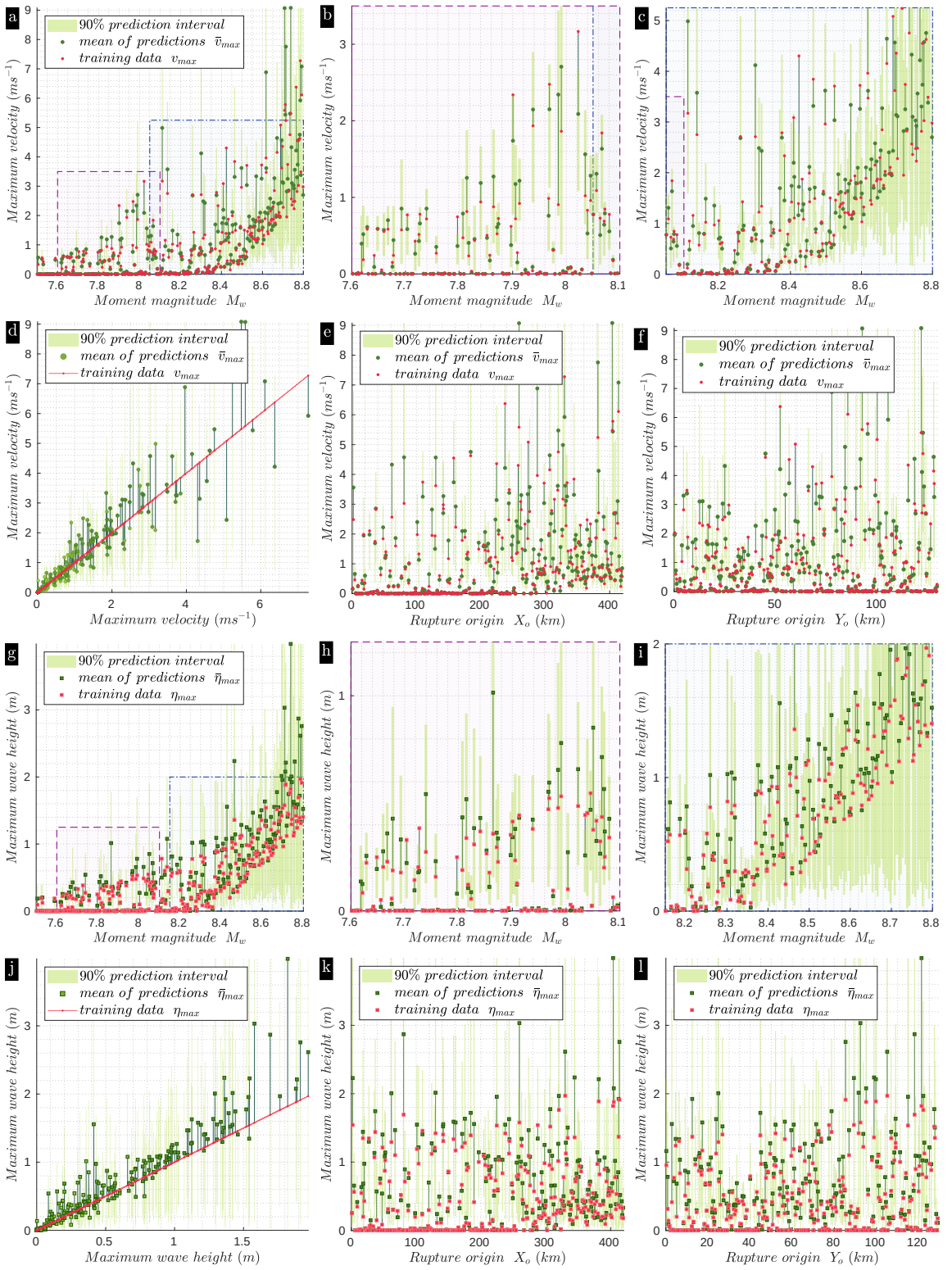


**Figure 10:** Emulator diagnostics. a) L-O-O for emulation of maximum velocity $v_{max}$ at a gauge in Karachi port (gauge no. 91 in Figures 12a-b). The vertical line segments connect the training data to its predicted counterpart. b) Enlargement of lower moment magnitude region in (a). c) Enlargement of higher moment magnitude region in (a). d) Same data in (a) plotted to show trend of predicted $\bar{v}_{max}$ with respect to training $v_{max}$. e) Same data in (a) but plotted with respect to $x$-coordinate of rupture origin $X_o$. f) Same data in (a) but plotted with respect to $y$-coordinate of rupture origin $Y_o$. g-l) Same as (a)-(f) but L-O-O for emulation of maximum height $\eta_{max}$ at gauge no. 91.

cheap approximation of the complex tsunami solvers, together with estimates of uncertainties in these predictions. In this study, the three input model parameters are moment magnitude ($M_w$) and rupture origin co-ordinates ($X_o, Y_o$) (Figure 3 inset). The inputs are transformed into effective seafloor displacements (Sections 2.1, 2.2 & 2.3). The consequent tsunamis are propagated till Karachi port (Section 2.4). The outputs of interest in our case are the maximum wave height ($\eta_{max}$) and maximum wave velocity ($v_{max}$) at $n_G$ (193) virtual gauge locations around the port.

Thus, the computer code (denoted by $\mathbb{M}$) simulates a multi-physics two-stage physical model, *i.e.* from slips $S^e$ to deformation $U^e$, then from $U^e$ to tsunami outputs $v$ and $\eta$. A design of computer experiments is an essential stage to create the data set used to construct the emulator. This consists of evaluations of the model (or computer runs of $\mathbb{M}$) at a finite number of locations in the space of input model parameters, together called the training set. We employ a Latin Hypercube Design (LHD) of size 300 for 3 parameters (Figures 9a-c). This is large enough to capture complex nonlinear combined sensitivities to the input parameters (*e.g.*, the influence of size and location in small and mid-size events closer to Karachi, or large regional variations in spatial distributions of slips), but still fits within our computational budget. The Gaussian Process (GP) emulator (denoted by $\mathcal{M}$) interpolates across the input-output points in the training set, and generates uncertain predictions elsewhere in the space of input parameters. The uncertainty in the predictions is modeled by a normal distribution whose mean and standard deviation are calculated using the Kriging formula (mean quantities denoted by $\bar{v}_{max}$ and $\bar{\eta}_{max}$). Derivations and exact equations can be found in Section 2 of Beck and Guillas (2016, Eqn. 2.4). GP emulation has been instrumental in successfully quantifying uncertainties in tsunami heights generated by landslides over the North Atlantic and the Western Indian Ocean as well as earthquakes over Cascadia (Salmanidou et al., 2017; Guillas et al., 2018; Salmanidou et al., 2019).

Maximum velocity magnitudes (and heights) are positive. In order to respect this physical constraint and not predict negative velocities (and heights), we feed the logarithm of $v_{max}$ (and $\eta_{max}$) into the construction of the emulator. Since the constructed emulator is now in the logarithmic scale, we transform the predicted quantities back to the original scale by accounting for the lognormal nature of the predicted distributions. Hence, the confidence intervals for the predictions, representing uncertainties, are all rendered positive, and naturally skewed in that direction, see Figure 10. Once the emulator is constructed, it needs to be validated before employing it for predictions. We turn to this aspect in the next section.

## 2.6. Emulator Diagnostics

In order to validate the quality of the emulation, we provide Leave-one-out (L-O-O) diagnostics here. As described in Section 2.5, our training set consists of 300 pairs of input-output quantities. In L-O-O, a reduced training set of 299 pairs is employed to build an emulator, which is then used to predict the output at inputs in the 1 pair that was left out. The predicted output (and its uncertainty) is compared to the actual output in the left out pair. This procedure

is repeated 300 times to cover all the pairs in the training set. These tests are passed by the emulator, as seen for predicted $\bar{v}_{max}$ in Figures 10a-f and $\bar{\eta}_{max}$ in Figures 10g-l. The comparison between the mean of predictions from the emulator $\mathcal{M}$ and the training data from the tsunami simulator $\mathbb{M}$ shows that the emulator approximates well the simulator. The vertical line segments connects the predicted means with the counterpart in the training data. More importantly, the uncertainties in the predicted mean, quantified in the form of 90% prediction intervals (green bars in Figure 10), represent well the uncertainties about these predictions (or are even slightly conservative) since around 90% or more of the outputs from the training set fall within these intervals.

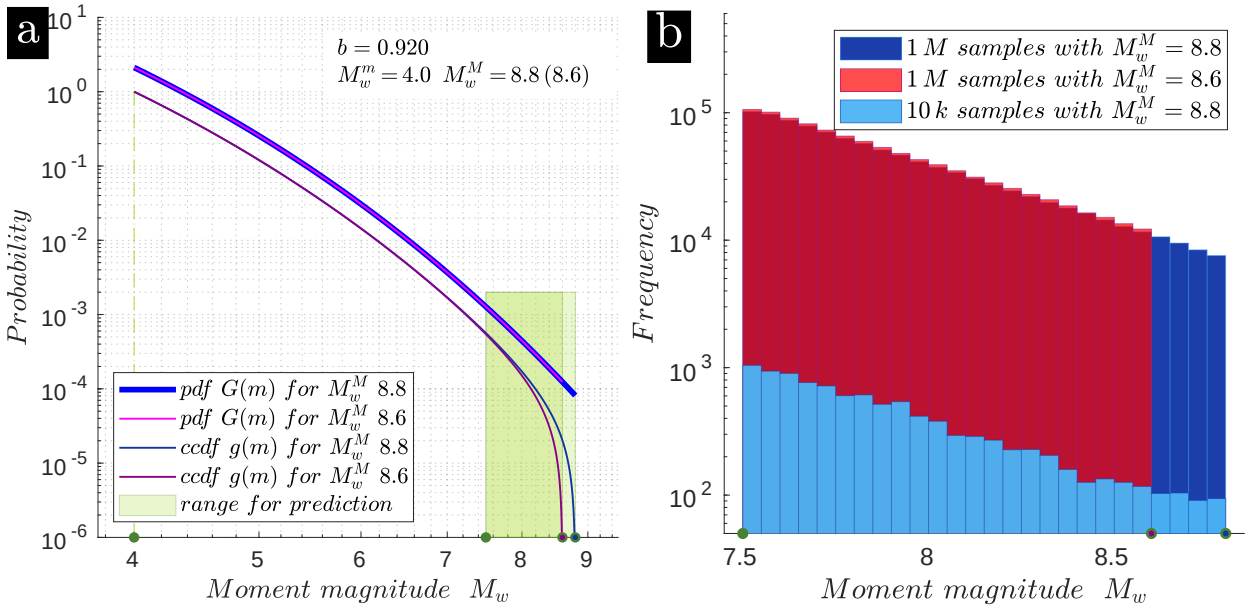


**Figure 11:** Emulator predictions. a) The Gutenberg-Richter (G-R) relation for the MSZ, showing probability and complementary cumulative distribution functions for two maximum moment magnitude assumptions, *viz.* 8.6 and 8.8. b) Histograms of 1 million (and 10,000) samples of $M_w$ used as inputs for predictions.

## 2.7. Emulator Predictions

Although the 300 simulations by itself may be considered to generate a good description of the hazard, a large number of scenarios are essential for a comprehensive probabilistic hazard assessment. Thus, we evaluate the model at $n_P$ (1 million) values of $\left(M_w, X_o, Y_o\right)$ at 193 virtual offshore gauges (locations shown in Figure 12). The constructed emulator is used to evaluate the model at inputs that are different from those in the training set. These evaluations are termed predictions. A prediction returns the mean value of the emulated quantity and a measure of inherent statistical error/uncertainty in the approximation, *e.g.* the standard deviation. Cumulatively, these 193 million predictions not only comprehensively cover the geography around Karachi port, but also exhaustively sweep through the entire range of events in the magnitude-frequency distribution. Additionally, such a high number of samples is also needed to

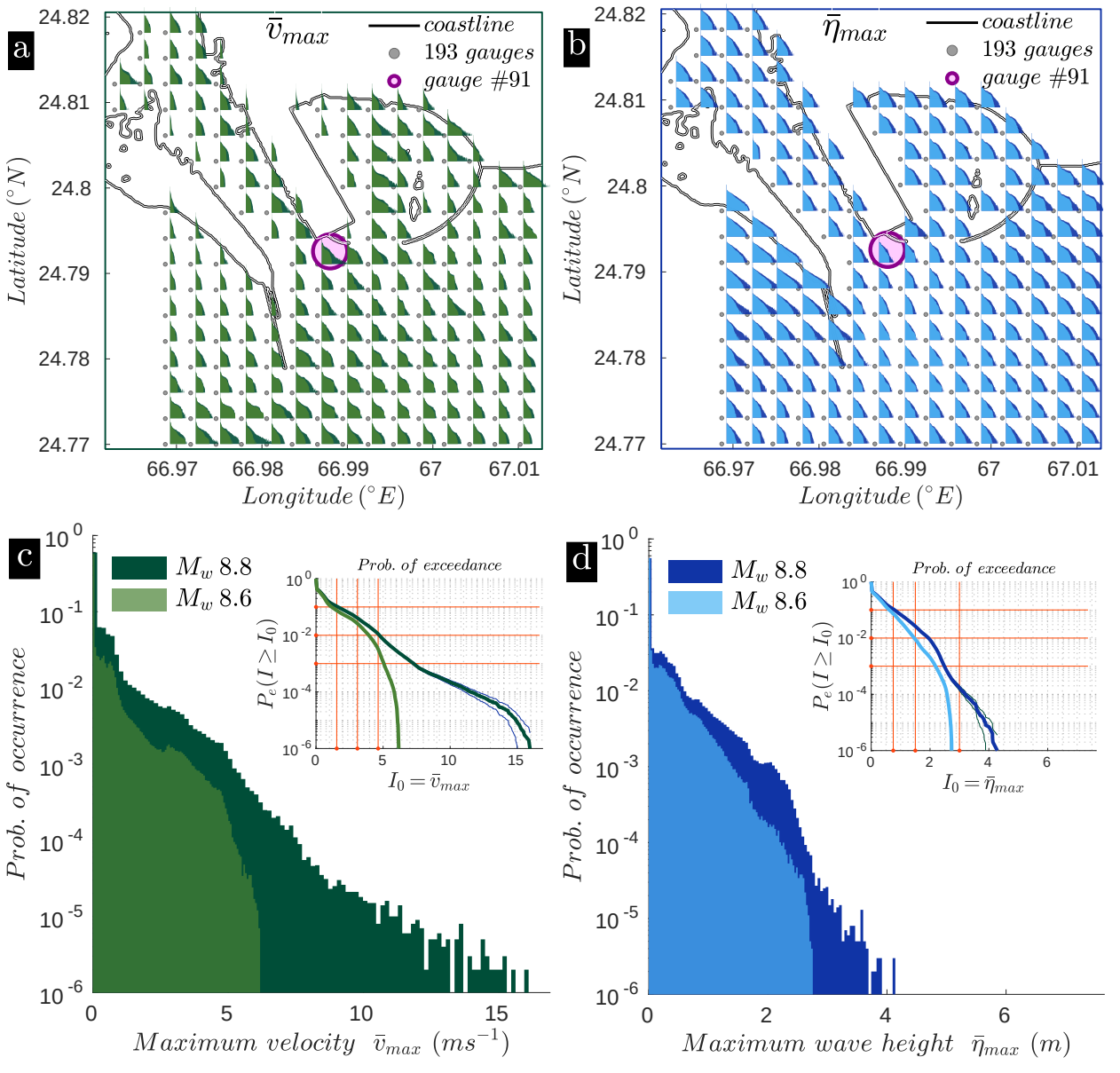


**Figure 12:** Raw output from 1 million predictions at 193 gauges. a) Histograms of 1 million predicted maximum velocities $\bar{v}_{max}$ at each of the 193 gauges. Each histogram has the same scale as (c). Histograms from maximum moment magnitude of 8.8 and 8.6 are superimposed. b) Same as (a) but for predicted maximum heights $\bar{\eta}_{max}$. c) Enlarged normalized histograms of predicted maximum velocities at gauge no. 91 comparing the two cases of different maximum moment magnitude. Inset shows probability of exceedance curves extracted from the histograms, with 99 % confidence interval. d) Same as (c) but for predicted maximum heights.

thoroughly explore the interplay among the three parameters in the input space of $(M_w, X_o, Y_o)$.

The 1 million $M_w$ values are sampled from the Gutenberg-Richter (G-R) distribution for the MSZ. Here, the probability distribution function (pdf) for the G-R relation is modeled as the doubly truncated exponential distribution (Cosentino

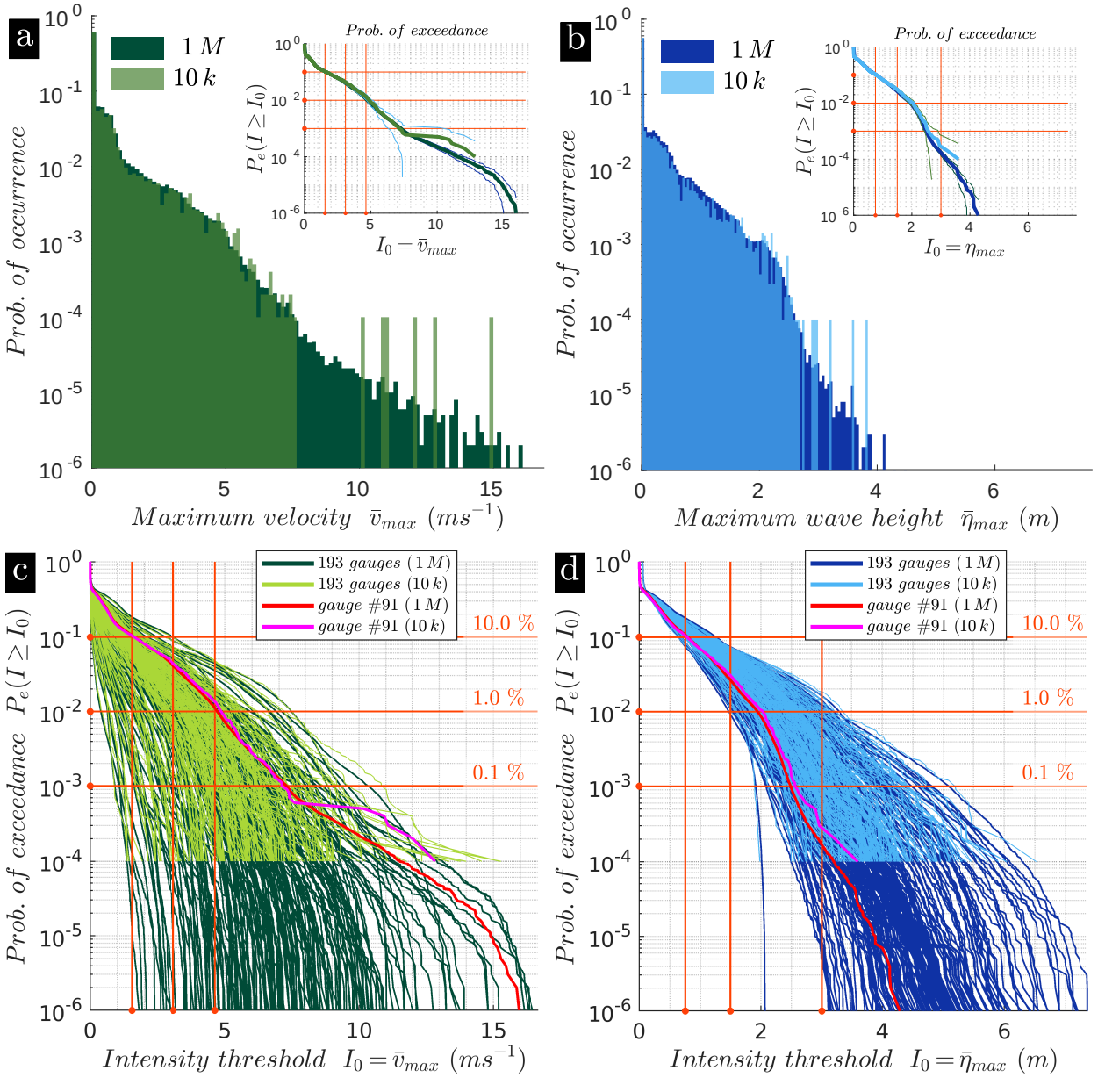


**Figure 13:** Hazard curves. a) Comparison of normalized histograms of 1 million and 10,000 predicted maximum velocities $\bar{v}_{max}$ at gauge no. 91. Inset shows probability of exceedance curves extracted from the histograms, with 99 % confidence intervals. b) Same as (a) but for predicted maximum heights $\bar{\eta}_{max}$. c) Probability of exceedance curves for predicted maximum velocities at 193 gauges. The curves for 10,000 predictions are superimposed over those from 1 million predictions. Curves for gauge no. 91 are marked out. Chosen values of probabilities and intensity thresholds used to generate hazard maps are marked as horizontal and vertical lines respectively. d) Same as (c) but for predicted maximum wave heights.

et al., 1977):

$$G(m) = \begin{cases} \dfrac{\beta e^{-\beta(m - M_w^m)}}{1 - e^{-\beta(M_w^M - M_w^m)}} & M_w^m \leq m \leq M_w^M \\ 0 & m > M_w^M \end{cases} \tag{15}$$

where $\beta = b \log_e 10$ and the lower $M_w^m$ and upper $M_w^M$ limits of truncation are 4 are 8.8 respectively. This rate parameter $b$ of 0.92 specific to the MSZ is taken from the most recent Earthquake Model of Middle East (EMME) database (Danciu et al., 2018, Table S1). The complementary cumulative distribution function (ccdf), also called probability of exceedance or survival function is then:

$$g(m) = \begin{cases} 1 - \dfrac{1 - e^{-\beta(m - M_w^m)}}{1 - e^{-\beta(M_w^M - M_w^m)}} & M_w^m \le m \le M_w^M \\ 0 & m > M_w^M \end{cases} \tag{16}$$

The $M_w$ for the 1 million events are then obtained by sampling the truncated distribution within our region of interest, *i.e.* $M_w$ 7.5 to $M_w$ 8.8 (see Figure 11a). The 1 million values of $\left(X_o, Y_o\right)$ are sampled from a uniform distribution defined over the rectangle $[0\ L^{max}] \times [0\ W^{max}]$ of area $420\,km \times 129\,km$. Assuming a reduction of maximum magnitude $M_w^M$ from 8.8 to 8.6 gives a perturbed G-R relation (Figure 11a). In this case, the 1 million samples come from the range $M_w$ 7.5 to $M_w$ 8.6. The histograms of 1 million samples for $M_w$ are shown in Figure 11b. It also shows $10,000$ samples from the range $M_w$ 7.5 to $M_w$ 8.8 for performing comparisons.

To be able to generate 1 million predictions, we employ the efficiently implemented Multiple-Output Gaussian Process emulator (MOGP)[6] from the Alan Turing Institute. Once the predictions are finished, we are left with two histograms (one each for $\bar{v}_{max}$ and $\bar{\eta}_{max}$) at every virtual gauge, each made up of 1 million samples of predicted quantity. The histograms are processed to extract $P_e\left(I(\boldsymbol{x}) \ge I_0\right)$, the probability of exceedance. $P_e$ is the probability of the tsunami having $I(\boldsymbol{x}) \ge I_0$ at a gauge $\boldsymbol{x}$. The intensity $I$ is the measure of hazard, *i.e.* either $\bar{v}_{max}$ or $\bar{\eta}_{max}$, and $I_0$ is the intensity threshold for the hazard quantity under consideration.

## 3. Results and Discussion

We first plot the raw output from the 1 million predictions, *i.e.* the histograms at 193 gauges in Figures 12a-b. At each gauge, two histograms are superimposed on each other. These correspond to the two G-R relations with varying maximum moment magnitude assumptions, *i.e.* $M_w^M$ 8.6 and $M_w^M$ 8.8 (Figure 11). The histograms also act as visual indicators for the measure of the hazard at the gauge, and will be cast as hazard maps in Figure 14. Near the tip of breakwaters and the mouth of the harbor, we observe relatively higher velocities than in other regions. We also observe a complementary relation between the histograms of velocities and wave heights: the gauges having thicker histograms for velocity have thinner histograms for wave heights and *vice versa*. These phenomena can also be observed in the snapshots in Figure 8 (compare panels (b) & (c) with (h) & (i) respectively).

As expected, there is a clear reduction of hazard when the maximum moment magnitude is reduced. For closer inspection, we enlarge the normalized histograms at gauge no. 91 in Figures 12c-d. Gauge no. 91 is located in the

[6] v0.2.0 available at *github.com/alan-turing-institute/mogp_emulator*

center of the map near the mouth of the port and is chosen since there is substantial spread of both maximum velocities and wave heights in its histograms. In Figure 12c, the normalized histograms for maximum velocity are plotted. The range of velocities for $M_w$ 8.8 extends till $\sim 16\, ms^{-1}$, while it extends to only $\sim 6.2\, ms^{-1}$ for $M_w$ 8.6. Thus, we observe a $\sim 61$ % reduction in maximum velocity hazard for a $M_w$ 0.2 reduction in maximum moment magnitude. In comparison, for the same reduction in maximum moment magnitude, the reduction in hazard from maximum wave height is only $\sim 38$ % (from $\sim 4.5\, m$ to $\sim 2.8\, m$ in Figure 12d). The probability of exceedance $P_e$ that is extracted from the histograms is plotted in the inset of the respective figure.

Figures 13a-b compare normalized histograms for 1 million and 10,000 samples of input parameters (see Figure 11b). The corresponding probability of exceedance $P_e$ plots with their 99% confidence intervals can be seen in the inset. In Figure 13a, we observe that the histogram corresponding to 10,000 predictions is curtailed around $7.5\, ms^{-1}$ and becomes very sparse for higher velocities. This is due to a deficit of samples that results in the isolated bars for higher velocities. This behaviour also translates into larger uncertainties (or wider confidence intervals) for estimates of low probabilities of $P_e$. In contrast, 1 million predictions adequately sweep through the entire range of velocities resulting in lower uncertainties (or narrower confidence intervals) for the tail probabilities. It may be noted that tail probabilities in the $P_e$ curve correspond to extreme events with higher velocities. Similar behaviour is seen in Figure 13b, where the deficit of samples is observed for maximum wave heights higher than $2.7\, ms^{-1}$ for the case of 10,000 predictions.

In Figures 13c-d, we plot the probability of exceedance curves extracted from the histograms of 1 million predictions for the 193 gauges. Superimposed on top are the $P_e$ curves for 10,000 predictions. The horizontal lines in the plots are the chosen values of probability of exceedance, $10^{-1}$, $10^{-2}$ and $10^{-3}$, progressively decreasing by an order of magnitude. The vertical lines in Figure 13c denote maximum velocities of 1.5, 3.1 and $4.6\, ms^{-1}$ (or 3, 6 and 9 knots respectively), values that demarcate categories of damage in Figure 1 of Lynett et al. (2014). The vertical lines in Figure 13c denote maximum wave heights of 0.75, 1.5 and $3\, m$. These values are used to construct hazard maps in Figure 14. In both Figures 13c-d, the reach of the $P_e$ curve is extended beyond the low probability of $10^{-4}$ to include even extreme events only in the case of 1 million predictions. Additionally, although the lower probabilities (around $10^{-4}$) have been made accessible by 10 thousand events, they require 1 million events for accurate resolution: with only 10,000 samples, both probabilities and quantities are overestimated between $10^{-3}$ and $10^{-4}$. Hence, being able to produce a very large number of predictions is crucial to hazard assessment. Only with the utilization of the emulator – needing only 300 simulations – are we able to afford realistic predictions of velocities and wave heights at high resolution.

Port hazard maps were developed for Crescent City, California (Lynett et al., 2014) and four sites in New Zealand (Borrero et al., 2015a). The hazard was represented on the maps by velocity zonations, a time-threshold metric and

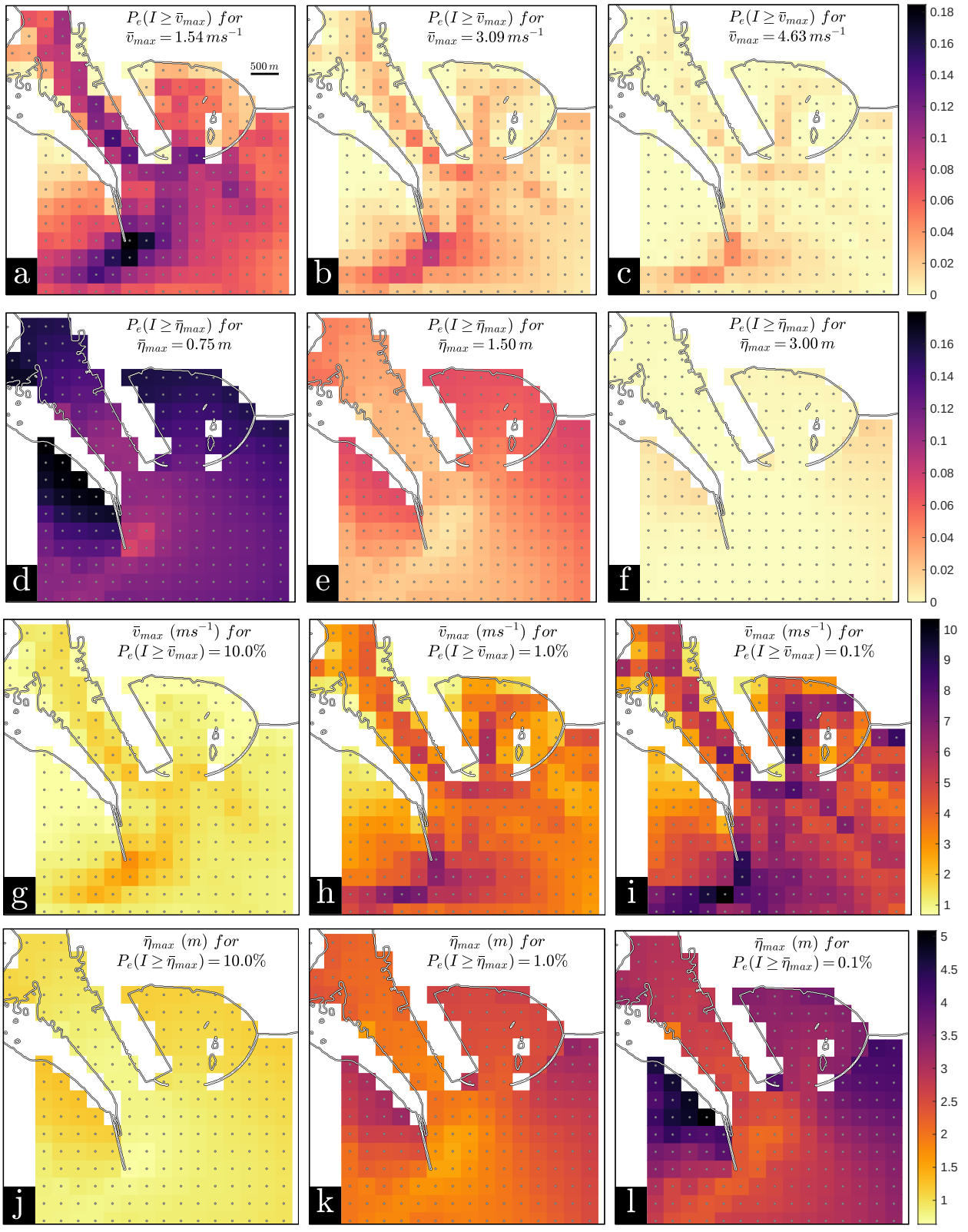


**Figure 14:** Hazard maps. a-c) Probability of exceedance at the 193 gauges for three chosen values of predicted maximum velocities $\bar{v}_{max}$. d-f) Predicted maximum velocities for three given probabilities of exceedance. g-l) Same as (a)-(f) but for predicted maximum wave heights $\bar{\eta}_{max}$.

safe depths for vessel evacuation. Here, the probability of exceedance curves in Figure 13 are cast as hazard maps in Figure 14, more along the lines of Gonzalez et al. (2013) and Park and Cox (2016). We plot the probability of exceedance at the 193 gauges on the map for the chosen values of maximum velocities in Figures 14a-c. Similar plots for chosen values of maximum wave heights are shown in Figures 14d-f. For both velocities and wave heights, the overall probability decreases as the intensity threshold increases. Specifically, the bulk of $P_e$ for maximum velocities is concentrated at the tip of breakwaters and along the dredged channel leading into the port (seen in port bathymetry, Figure 6j), as also observed in (Lynett et al., 2012). This is also supported by the patterns of localised higher maximum velocities in Figures 8a & d. In contrast, the spatial distribution of $P_e$ for maximum wave height shows a complementary behaviour and is more spread out.

Conversely, for chosen probabilities of exceedance, the corresponding hazard threholds at the gauges are plotted in Figures 14g-l. As expected, the overall intensity thresholds increase with decrease in probability of exceedance. Again, the bulk of the maximum velocity threshold is concentrated at the tip of breakwaters and along the dredged channel (Figures 14g-i). Here too, we see a complementary behaviour for maximum wave height in Figures 14j-l.

Arcos and LeVeque (2015) found that velocities have more spatial variation than heights. Dengler and Uslu (2011) showed increased sensitivity of velocities to port configurations, compared to wave heights. The larger spatial variation of velocities in Figure 13c compared to wave heights in Figure 13d is evident in the probability of exceedance plotted for all the gauges. This can be attested in Figures 12a-b, where the bulkiness of velocity histograms varies spatially much more than that of the heights. Additionally, at a given gauge, we observe that the spread of velocities is much more than those of the heights for the same set of earthquake scenarios, *e.g.* compare Figures 12a-b for gauge no. 91. These behaviours can also be deduced for individual runs from the spatial variations of maximum velocity and wave height is Figure 8 (compare panels (a) & (d) with (g) & (j) respectively).

The probability of exceedance extracted in this work acts as the basic input for common hazard outputs of probability of occurrence (and return periods), especially the $\sim$2475 year mean return period for the Maximum Considered Tsunami (MCT) as laid out in Chapter 6 of ASCE 7-16 (Chock, 2016). It also feeds into loss estimation functions (Muhari et al., 2015). But a full probabilistic assessment would ideally need to include further sources of uncertainties. These include layers of uncertainties that are either epistemic or aleatoric in nature. Epistemic uncertainties include the scaling relation, and the Gutenberg-Richter approximation of the occurrence-magnitude relationship (Davies et al., 2018), *i.e.* both the maximum moment magnitude and the *b*-value. The major influence of the maximum magnitude was illustrated in initial work by Hoechner et al. (2016), but for a simplified tsunami modeling strategy. Here, we only assess two cases, for $M_w^M$ 8.6 and $M_w^M$ 8.8. Uncertainties in the bathymetry near shore have also been shown to have a large influence on tsunamis at the shore (Liu and Guillas, 2017). Combining the tools of dimension reduction and emulation, such a modeling of the epistemic uncertainty would be beneficial to include.

Aleatoric uncertainties in the variations of the geometry in the seafloor uplift and subsidence can be readily incorporated. An alternative to our slip profile generation is to directly parameterize the co-seismic deformation profile using 3 parameters as in Guillas et al. (2018) (or more) to vary the geometry more freely and be more realistic. The Okada model that transforms the slips to the vertical deformation is then bypassed. This route is quite attractive since it allows the creation of very realistic deformation patterns with a fixed number of parameters, and does away with the dependency of the deformation/slip on the resolution of the segmentation (shown in Figure 3b inset).

Our work uniformly samples the 1 million samples for rupture origin co-ordinates (another aleatoric uncertainty). However, a recent spatial distribution of locking has been made available for the MSZ (Frohling and Szeliga, 2016). It would be even more realistic to sample the rupture origin coordinates using the locking distribution, since zones of high locking act as a major cause for earthquake reoccurence as recently hypothesised in Moernaut et al. (2018). The locations could be further distributed based on the depth dependent rigidity (Scala et al., 2019).

Randomness in tide levels at the time of impact (consequent changes of up to 25% reported in Ayca and Lynett (2016)) could be included, as well as the numerical error in the approximation of the currents since our depth-averaged model is 2-D but 3-D modeling will increase precision, and account for vertical vorticity (Lynett et al., 2017; Lynett, 2016). Better designs of computer experiments than the Latin Hypercube Design used here could be employed to reduce uncertainties in the emulator's approximation, such as sequential design (Beck and Guillas, 2016) already used for tsunamis with success and is now implemented in an advanced computational workflow.

Instead of investigating a range of scenarios, if one only wants to examine the maximum wave height in order to build defences for instance, a recent surrogate-based optimization could be pursued whereby the design of experiment is combined with a search for the maximum, saving large quantities of computational time and increasing accuracy due to the focus on the optimization (Mathikolonis et al., 2019). To be able to emulate a sequence of multiple models of seabed deformation and tsunami propagation, and possibly a 3-D model of currents locally, a new approach, called integrated emulation (Ming and Guillas, 2019) allows even better designs where the most influential models are run more times where it matters, and where the integrated emulator propagates uncertainties with higher fidelity by taking into account the intermediate models in the system of simulators. This approach has the potential to enable fully realistic end-to-end coupling of 3-D earthquake sources models with tsunami models (Ulrich et al., 2019).

## 4. Conclusions

In this paper, we provide a novel end-to-end quantification of uncertainties of future earthquake-generated tsunamis heights and currents in the MSZ:

1. We replace the complex, expensive high-resolution tsunami simulator by a functionally simple, cheap statistical emulator trained using 300 tsunami simulations at 10 $m$ mesh resolution in the vicinity of the port. We propagate

uncertainties from the Gutenberg-Richter relation to tsunami impacts of maximum velocities and wave heights in the port area of Karachi, Pakistan. We observe maximum (extreme event) velocities and wave heights of up to $16\,ms^{-1}$ and $8\,m$ respectively for the range $M_w$ 7.5 – 8.8 (Figure 12).

2. We perform the largest emulation using 1 million predictions/source scenarios. To our knowledge, this is the first large-scale uncertainty quantification of earthquake-generated tsunami current hazard. We are able to display the necessity of this very large number of predictions for resolving very low probabilities of exceedance ($< 10^{-3}$) - very high impact extreme events ($v_{max} > 7.5\,ms^{-1}$ and $\eta_{max} > 3\,m$) with tighter uncertainties (Figure 13).
3. We observe that reduction in hazard due to a reduction in maximum moment magnitude is more for velocities than wave heights. Near the mouth of the harbor, the reduction in hazard is $\sim 61\,\%$ for maximum velocity, but only $\sim 38\,\%$ for maximum wave height (corresponding to a reduction in maximum moment magnitude from 8.8 to 8.6) (Figure 13c).
4. We generate the first area-wide probabilistic hazard maps of tsunami currents from 1 million predicted scenarios at the Karachi port (Figures 14a-f). It shows patterns that are geophysically meaningful and important for the next steps of disaster risk reduction. We identify concentrations of high probability of exceedance around the port for given intensity threshold (a maximum of $\sim 18\,\%$, $10\,\%$ and $4\,\%$ for 3, 6 and 9 knots respectively) (Figures 14a-c). Conversely, the same regions also have high intensity thresholds given probability of exceedance (a maximum of $\sim 3.1$, 7.5 and $10.3\,ms^{-1}$ for $10\,\%$, $1\,\%$ and $0.1\,\%$ respectively) (Figures 14d-f). Overall, without our large-scale emulation, such outputs would be impractical to produce due to computational costs.
5. We display more spatial variations for maximum velocity compared to wave heights around the port and their complementary behaviour for the aggregate of 1 million scenarios (Figures 8, 12, 13 and 14).

## A. Slip Profile Generation

Select the dimension ($h_s$) of a FF segment based on: (i) computational effort required – increases as $h_s$ decreases, along $O\left(n_F^2\right) \sim O\left(h_s^{-2}\right)$, (ii) fidelity to the scaling relation (Figure 3b inset) – earthquake dimensions are resolved to $O\left(h_s\right)$ (Figure 3b). We select $h_s \sim 5\,km$, which for the overall FF dimensions of $L^{max} \sim 420\,km$ and $W^{max} \sim 129\,km$ results in 2295 segments. With the segment dimension $h_s$, use the scaling relation to determine the minimum $M_w$ that can be accommodated on the FF. To resolve the slip profile adequately, we require a fault to span a minimum of 4 segments in both the length and width directions. This results in a minimum $M_w$ of 6.32. This is sufficient as our region of investigation starts at $M_w^{min} = 7.5$. For the FF model of area $L^{max} \times W^{max}$, use the scaling relation to determine the maximum $M_w$ that can be accommodated on the FF. We get the maximum $M_w$ as $M_w^{sat} = 8.65$ (Figure 3a). Since our region of investigation is till $M_w$ 8.8, for ruptures with $M_w > M_w^{sat}$, we saturate the slip on the fault with $M_w^{sat}$. Algorithm 1 and Figures 4b-d detail the slip profile generation given the input parameter $\left(M_w, X_o, Y_o\right)$.

**Algorithm 1** Slip profile generation

1: For a given earthquake moment magnitude $M_w$, and rupture origin co-ordinates $\left(X_o, Y_o\right)$ (Figure 3a inset); find the rupture length $L$ and width $W$ from the scaling relation. The co-ordinates have their origin as the south-west corner of the FF (Figure 3a inset).
2: Fit the fault rectangle of size $L \times W$ into the FF. There are two possibilities with the rupture origin $\left(X_o, Y_o\right)$ being located at :
(i) the centre of the fault and equidistant from the boundaries of the fault rectangle, *i.e.* with distances $L/2$ and $W/2$.
(ii) not the centre of the fault. In this case, $\left(X_o, Y_o\right)$ is at different distances from the boundaries of the fault rectangle.
3: Use Eqn. 3 to construct the lobes $\phi\left(x; r_E, \alpha\right)$ and $\phi\left(x; r_W, \alpha\right)$ and form the bi-lobed kernel function for fault length $\Phi\left(x; r_W, r_E, \alpha\right)$ (Figure 4b). Similarly, form the bi-lobed kernel function for fault width $\Phi\left(x; r_N, r_S, \alpha\right)$ by constructing the lobes $\phi\left(x; r_N, \alpha\right)$ and $\phi\left(x; r_S, \alpha\right)$ (Figure 4d). $r_E$, $r_W$, $r_N$ and $r_S$ are the distances of earthquake origin from the eastern, western, northern and southern sides of the fault rectangle.
4: Use Eqn. 4 to construct the tensor product $\Phi^{\otimes}$ of the two bi-lobed kernel functions in the previous step. $\Phi^{\otimes}$ will entirely reside within the fault rectangle and will become 0 at its boundaries (Figure 4c).
5: Multiply the values of $\Phi^{\otimes}$ at the centres of each segment (*i.e.* $\Phi_i^{\otimes}$) with a factor $M_w \left(\sum_{i=1}^{n_F} \mu l_i w_i \Phi_i^{\otimes}\right)^{-1}$ to get the slip $S_i$ on the segment. This normalization results in the slips in the fault rectangle to have a combined moment magnitude of $M_w$.

## B. Merging Bathymetry Data from Hydrographic Chart, SRTM, GEBCO and Satellite Imagery

The four data sets that are used to create the merged bathymetry for computational mesh generation (Section 2.4.2) and tsunami simulations (Section 2.4) are at different resolutions – $\sim 1'' \sim 30\,m$ (digitized hydrographic charts and SRTM v3), $\sim 15'' \sim 450\,m$ (GEBCO 2019), and $\sim 10\,m$ (coastline features in satellite imagery from Google Earth). The digitized chart data is available in the domain of interest (DOI) $[66.9332, 67.0168]^\circ E \times [24.7666, 24.8334]^\circ N$. The cosine-tapered Tukey window used in the merging process is given by:

$$\theta\left(x, r_c\right) = \begin{cases} \frac{1}{2}\left\{1 + \cos\left(\frac{2\pi}{r_c}\left[x - r_c/2\right]\right)\right\} & 0 \le x \le \frac{r_c}{2} \\ 1 & \frac{r_c}{2} \le x \le 1 - \frac{r_c}{2} \\ \frac{1}{2}\left\{1 + \cos\left(\frac{2\pi}{r_c}\left[x - 1 + r_c/2\right]\right)\right\} & 1 - \frac{r_c}{2} \le x \le 1 \end{cases} \tag{B.1}$$

where $r_c$ is the ratio of length of cosine-taper to the total window length of 1. Shifted and dilated versions of $\theta$ are used to create the tensor product:

$$\Theta\left(x - x_p, y - y_p, d_x, d_y, r_c^x, r_c^y\right) = \theta\left(\frac{x - x_p}{d_x}, r_c^x\right) \otimes \theta\left(\frac{y - y_p}{d_y}, r_c^y\right) \tag{B.2}$$

where $\left(x_p, y_p\right)$ and $d_x \times d_y$ are co-ordinates of the centre and area of the DOI respectively, whilst $\left(r_c^x, r_c^y\right)$ are the cosine-fractions along the length and width of the DOI. Algorithm 2 and Figure 6 detail the procedure used for merging the different bathymetries.

**Algorithm 2** Merging bathymetry data

1: Up-sample the hydrographic chart data and GEBCO bathymetry in the DOI on a rectangular grid having a resolution of the computational mesh ($\sim 10\,m$) (Figures 6a & d respectively).
2: Integrate the polygonal domains of resolved coastline features into up-sampled bathymetry by filling land areas with a positive constant ($2\,m$) (Figure 6b).
3: Interpolate the SRTM data for land onto the grid. If SRTM data exists on the water area after integration of port features, discard the SRTM data there (Figure 6c).
4: Construct tensor product of cosine-tapered Tukey windows ($\Theta$) and its complement ($1-\Theta$) with cosine fractions $r_c^x = r_c^y = 10\,\%$ (Figures 6f & 6g respectively).
5: Multiply hydrographic chart data integrated with port coastline features and SRTM data (Figure 6c) with $\Theta$ (Figure 6f) to get windowed merged bathymetry (Figure 6h). The data at the start of the taper is used for the tapered region.
6: Multiply GEBCO 2019 data (Figure 6d) with $1-\Theta$ (Figure 6g) to get windowed GEBCO bathymetry (Figure 6i).
7: Add windowed merged bathymetry (Figure 6h) with windowed GEBCO bathymetry (Figure 6i) to get the final merged bathymetry (Figure 6j).

## C. Localised Non-Uniform Unstructured Mesh

The mesh sizing function $h$ that is fed into Gmsh is constructed in three stages, *viz.* offshore, onshore and port regions. For offshore mesh, the design criteria is based on the bathymetry $b$ (Figure 7a inset). Some more steps are required after the definition of $h_\lambda$ in Eqn. 14 of Section 2.4.2. The mesh sizing $h_\lambda$ defined in Eqn. 14 may turn out to be too steep (green curve in Figure 7a), or having a a high gradient with respect to the bathymetry $b$. A reduction is gradient is achieved by interpolating between the triangle size $\lambda_o/n_h$ at $b_o$ and the minimum mesh size $h_m$ at the coast, *i.e.* $b=0$ (red curve in Figure 7a):

$$h_I\left(b\right) = b\left(\boldsymbol{x}\right) * \left(\lambda_o/n_h - h_m\right) / \left(b_o - 0\right) + h_m \tag{C.1}$$

The mesh sizing function $h\left(b\right)$ is then given by the minimum:

$$h\left(b\right) = \min\left(h_\lambda\left(b\right), h_I\left(b\right)\right) \tag{C.2}$$

Next, the design criteria for the onshore mesh sizing function $h\left(\pi\right)$ is based on the coast proximity $\pi\left(\boldsymbol{x}\right)$ defined as the minimum distance of a point $\boldsymbol{x}$ from the coastline $\mathcal{C}$ of the merged bathymetry (Figure 7b inset):

$$\pi\left(\boldsymbol{x}\right) = \min_{\boldsymbol{x}_c \in \mathcal{C}} \left\|\boldsymbol{x} - \boldsymbol{x}_c\right\|_2 \tag{C.3}$$

The mesh sizing function is broken into three regions, *viz.* inundation, stretch and blow-up regions (Figure 7b). In the inundation region which extends inland for a distance $\pi_I$ (2.5 $km$) from the coast, the mesh size is prescribed as the minimum mesh size $h_m$ (500 $m$). Thus, the inundation region acts as a smooth transitioning region between the onshore and offshore mesh. Further inland away from the inundation region, we require the triangle sizes to explode quickly to the maximum mesh size $h_M$ (25 $km$). This region is called the blow-up region (from $\pi_S$ to $\pi_B$ in Figure 7b). Since such a transition needs to happen in a smooth manner, we introduce the stretch region between the end of the inundation region and the beginning of the blow-up region (from $\pi_I$ to $\pi_S$ in Figure 7b). In the stretch region the triangle size transitions from $h_m$ to $h_S$ (10 $km$). To prescribe mesh sizes in the stretch region, we define the *size ratio* $\rho$ (= 1.3) to be the ratio of sizes of adjacent triangle in the mesh (also called *grading gauge* in Legrand et al. (2006)). The stretch distance $\pi_S - \pi_I$ is calculated as:

$$\pi_S - \pi_I = h_m + \rho h_m + \rho^2 h_m + \ldots + \rho^{n_S} h_m \tag{C.4}$$

Eqn. C.4 is a geometric series that approximates the distance by summing up the sizes of $n_S + 1$ triangles, lined up end-to-end in a straight line, progressively increasing in size by a factor of $\rho$ (Legrand et al., 2006), starting from $h_m$ to $\rho^{n_S} h_m$. Equating the last term to $h_S$, solves for integer $n_S$ as:

$$n_S = \lceil \log_\rho \left( \frac{h_S}{h_m} \right) \rceil \tag{C.5}$$

where $\lceil \cdot \rceil$ denotes the ceiling function. Similarly, the blow-up distance $\pi_B - \pi_S$ is calculated as:

$$\pi_B - \pi_S = h_S + \rho h_S + \rho^2 h_S + \ldots + \rho^{n_B} h_S \tag{C.6}$$

Similar to Eqn. C.4, Eqn. C.6 is a geometric series summing up the sizes of $n_B + 1$ triangles, progressively increasing in size from $h_S$ to $\rho^{n_B} h_S$, by a factor of $\rho$. Equating the last term to $h_M$, solves for integer $n_B$ as:

$$n_B = \lceil \log_\rho \left( \frac{h_M}{h_S} \right) \rceil \tag{C.7}$$

The mesh sizing function is specified to Gmsh on a background rectangular mesh. The resolution of the background mesh is half the resolution of GEBCO grid, *i.e.* ∼210 $m$, sufficient for specifying the $h_m$ of 500 $m$. Each of the above mesh sizings for the inundation, stretch and blow-up regions need to be specified on the background mesh. The number of levels mentioned in Figure 7b are the number of grids in the background mesh needed to specify mesh sizes in the respective region.

Finally, the mesh sizing function is constructed in the vicinity of the port (Figure 7h-j). The strategy followed is similar to offshore mesh sizing, but instead of the proximity to coast, the radial distance from the centre $\left(x_p, y_p\right)$ of the DOI (or port) is used. A $\rho^p$ of 1.05 is chosen for a very smooth transition of mesh. The mesh sizing is fixed at $h_m^p$ (10 $m$) for the DOI where the resolved bathymetry is available. The resolution of background mesh near the port is kept at 10 $m$, *i.e.* at least same as $h_m^p$. In increasing radii extending outwards from the DOI, the mesh sizing increases similar to Eqn. C.4 but iteratively with increasing number of terms. The iterative procedure is employed to ensure that there is a smooth merging of the mesh sizing function at the port with existing offshore and onshore mesh sizing functions.

## CRediT authorship contribution statement

**Devaraj Gopinathan:** Conceptualization, Methodology, Software, Validation, Investigation, Resources, Data Curation, Writing - Original Draft, Writing - Review & Editing, Visualization, Funding acquisition. **Mohammad Heidarzadeh:** Conceptualization, Methodology, Data Curation, Writing - Review & Editing, Visualization, Funding acquisition. **Serge Guillas:** Conceptualization, Methodology, Validation, Resources, Writing - Original Draft, Writing - Review & Editing, Supervision, Project administration, Funding acquisition.

## Acknowledgments

DG and SG were supported by the Alan Turing Institute under the EPSRC grant [EP/N510129/1] for the project '*Uncertainty Quantification of multi-scale and multiphysics computer models: applications to hazard and climate models*'. DG was partially funded by the Royal Society-SERB Newton International Fellowship [NF151483] for the project '*Inverse modeling of Tsunami Source Characterization and its Use in Early Warnings*'. DG, MH and SG acknowledge funding from the NERC grant [NE/P016367/1] '*Tsunami risk for the Western Indian Ocean: steps toward the integration of science into policy and practice*' under the Global Challenges Research Fund: Building Resilience programme. This work has been performed using resources provided by the Cambridge Tier-2 system (CSD3 Wilkes2) operated by the University of Cambridge Research Computing Service funded by EPSRC Tier-2 capital grant EP/P020259/1. The authors would like to acknowledge the use of the University of Oxford Advanced Research Computing (ARC) facility (JADE) in carrying out this work (doi.org/10.5281/zenodo.22558). Preparative simulations were performed on the EMERALD High Performance Computing facility provided via the EPSRC funded Centre for Innovation (EP/K000144/1 and EP/K000136/1), owned and operated by the e-Infrastructure South Consortium formed by the universities of Bristol, Oxford, Southampton and UCL in partnership with STFC Rutherford Appleton Laboratory. DG acknowledges support from Eric Daub and Oliver Strickson for active development of MOGP UQ suite, Daniel Giles for improvements to second order FV scheme and boundary conditions in VOLNA-OP2, and István Reguly

for smooth installation and running of VOLNA-OP2 on CSD3. We also acknowledge fruitful discussions with Deyu Ming and Mariya Mamajiwala on truncated G-R distribution and prediction intervals for L-O-O diagnostics, Frédéric Dias on meshing strategies and sediment amplification curve, Theodoros Mathikolonis on emulation, and Simon Day, Kusala Rajendran and C.P. Rajendran on seismicity of MSZ. We thank David H. Hickcox for permission to reproduce his photograph of *Maersk Mandraki* in Figure 1d.

## References

Allen, T.I., Hayes, G.P., 2017. Alternative rupture-scaling relationships for subduction interface and other offshore environments. Bulletin of the Seismological Society of America 107, 1240–1253. doi:10.1785/0120160255.

Arcos, M.E.M., LeVeque, R.J., 2015. Validating velocities in the GeoClaw tsunami model using observations near Hawaii from the 2011 Tohoku tsunami. Pure and Applied Geophysics 172, 849–867. doi:10.1007/s00024-014-0980-y.

Ayca, A., Lynett, P.J., 2016. Effect of tides and source location on nearshore tsunami-induced currents. Journal of Geophysical Research: Oceans 121, 8807–8820. doi:10.1002/2016JC012435.

Battaglia, M., Cervelli, P., Murra-Muraleda, J., 2012. Modeling crustal deformation_A catalog of deformation models and modeling approaches. US Geological Survey Techniques and Methods , 37–85.

Battaglia, M., Cervelli, P.F., Murray, J.R., 2013. dMODELS: A MATLAB software package for modeling crustal deformation near active faults and volcanic centers. Journal of Volcanology and Geothermal Research 254, 1 – 4.

Beck, J., Guillas, S., 2016. Sequential design with Mutual Information for Computer Experiments (MICE): Emulation of a tsunami model. SIAM/ASA Journal on Uncertainty Quantification 4, 739–766. doi:10.1137/140989613.

Blaser, L., Krüger, F., Ohrnberger, M., Scherbaum, F., 2010. Scaling relations of earthquake source parameter estimates with special focus on subduction environment. Bulletin of the Seismological Society of America 100, 2914–2926. doi:10.1785/0120100111.

Borrero, J.C., Goring, D.G., Greer, S.D., Power, W.L., 2015a. Far-field tsunami hazard in New Zealand ports. Pure and Applied Geophysics 172, 731–756. doi:10.1007/s00024-014-0987-4.

Borrero, J.C., Lynett, P.J., Kalligeris, N., 2015b. Tsunami currents in ports. Philosophical Transactions of the Royal Society A: Mathematical, Physical and Engineering Sciences 373, 20140372. doi:10.1098/rsta.2014.0372.

Byrne, D.E., Sykes, L.R., Davis, D.M., 1992. Great thrust earthquakes and aseismic slip along the plate boundary of the Makran Subduction Zone. Journal of Geophysical Research: Solid Earth 97, 449–478. doi:10.1029/91JB02165.

Chock, G.Y.K., 2016. Design for tsunami loads and effects in the ASCE 7-16 standard. Journal of Structural Engineering 142, 04016093. doi:10.1061/(ASCE)ST.1943-541X.0001565.

Cosentino, P., Ficarra, V., Luzio, D., 1977. Truncated exponential frequency-magnitude relationship in earthquake statistics. Bulletin of the Seismological Society of America 67, 1615–1623.

Danciu, L., et al., 2018. The 2014 earthquake model of the Middle East: seismogenic sources. Bulletin of Earthquake Engineering 16, 3465–3496. doi:10.1007/s10518-017-0096-8.

Davies, G., et al., 2018. A global probabilistic tsunami hazard assessment from earthquake sources. Geological Society, London, Special Publications 456, 219–244. doi:10.1144/SP456.5.

Dengler, L., Uslu, B., 2011. Effects of harbor modification on Crescent City, California's tsunami vulnerability. Pure and Applied Geophysics 168, 1175–1185. doi:10.1007/s00024-010-0224-8.

731 Dias, F., Dutykh, D., ÓBrien, L., Renzi, E., Stefanakis, T., 2014. On the modelling of tsunami generation and tsunami inundation. Procedia IUTAM
732 10, 338 – 355. doi:10.1016/j.piutam.2014.01.029. mechanics for the World: Proceedings of the 23rd International Congress of Theoretical
733 and Applied Mechanics, ICTAM2012.
734 Dutykh, D., Dias, F., 2010. Influence of sedimentary layering on tsunami generation. Computer Methods in Applied Mechanics and Engineering
735 199, 1268 – 1275. doi:10.1016/j.cma.2009.07.011. multiscale Models and Mathematical Aspects in Solid and Fluid Mechanics.
736 Dutykh, D., Poncet, R., Dias, F., 2011. The VOLNA code for the numerical modeling of tsunami waves: Generation, propagation and inundation.
737 European Journal of Mechanics - B/Fluids 30, 598 – 615. doi:10.1016/j.euromechflu.2011.05.005. special Issue: Nearshore Hydrody-
738 namics.
739 Frohling, E., Szeliga, W., 2016. GPS constraints on interplate locking within the Makran subduction zone. Geophysical Journal International 205,
740 67–76. doi:10.1093/gji/ggw001.
741 GEBCO Bathymetric Compilation Group 2019, 2019. The GEBCO_2019 Grid - a continuous terrain model of the global oceans and land. doi:10/
742 c33m.
743 Geuzaine, C., Remacle, J.F., 2009. Gmsh: A 3-D finite element mesh generator with built-in pre- and post-processing facilities. International
744 Journal for Numerical Methods in Engineering 79, 1309–1331. doi:10.1002/nme.2579.
745 Giles, D., Kashdan, E., Salmanidou, D.M., Guillas, S., Dias, F., 2020. Performance analysis of Volna-OP2 – massively parallel code for tsunami
746 modelling. arXiv preprint arXiv:2002.04889 .
747 Gonzalez, F.I., LeVeque, R.J., Adams, L.M., 2013. Probabilistic Tsunami Hazard Assessment (PTHA) for Crescent City, CA. Final Report for
748 Phase I. Technical Report. University of Washington Department of Applied Mathmatics.
749 Grezio, A., Babeyko, A., Baptista, M.A., Behrens, J., Costa, A., Davies, G., Geist, E.L., Glimsdal, S., González, F.I., Griffin, J., Harbitz, C.B.,
750 LeVeque, R.J., Lorito, S., Løvholt, F., Omira, R., Mueller, C., Paris, R., Parsons, T., Polet, J., Power, W., Selva, J., Sørensen, M.B., Thio, H.K.,
751 2017. Probabilistic tsunami hazard analysis: Multiple sources and global applications. Reviews of Geophysics 55, 1158–1198. doi:10.1002/
752 2017RG000579.
753 Guillas, S., Sarri, A., Day, S.J., Liu, X., Dias, F., et al., 2018. Functional emulation of high resolution tsunami modelling over Cascadia. The Annals
754 of Applied Statistics 12, 2023–2053. doi:10.1214/18-AOAS1142.
755 Hanks, T.C., Kanamori, H., 1979. A moment magnitude scale. Journal of Geophysical Research: Solid Earth 84, 2348–2350. doi:10.1029/
756 JB084iB05p02348.
757 Hasan, H., Lodhi, H., LeVeque, R., Lodhi, S., Ahmed, S., 2017. Assessing tsunami risk to Karachi Port through simulation of currents that were
758 reportedly produced there by the 1945 Makran tsunami, in: Proceedings of the 16th world conference on earthquake engineering, Santiago,
759 Chile.
760 Hayes, G.P., 2018. Slab2 - A Comprehensive Subduction Zone Geometry Model: U.S. Geological Survey data release. doi:10.5066/F7PV6JNV.
761 Hayes, G.P., Moore, G.L., Portner, D.E., Hearne, M., Flamme, H., Furtney, M., Smoczyk, G.M., 2018. Slab2, a comprehensive subduction zone
762 geometry model. Science 362, 58–61. doi:10.1126/science.aat4723.
763 Heidarzadeh, M., Kijko, A., 2011. A probabilistic tsunami hazard assessment for the Makran subduction zone at the northwestern Indian Ocean.
764 Natural Hazards 56, 577–593. doi:10.1007/s11069-010-9574-x.
765 Heidarzadeh, M., Pirooz, M.D., Zaker, N.H., Yalciner, A.C., Mokhtari, M., Esmaeily, A., 2008. Historical tsunami in the Makran Subduction Zone
766 off the southern coasts of Iran and Pakistan and results of numerical modeling. Ocean Engineering 35, 774 – 786. doi:10.1016/j.oceaneng.
767 2008.01.017.
768 Heidarzadeh, M., Satake, K., 2014. Possible sources of the tsunami observed in the northwestern Indian Ocean following the 2013 September 24

769 Mw 7.7 Pakistan inland earthquake. Geophysical Journal International 199, 752–766. doi:10.1093/gji/ggu297.

770 Hoechner, A., Babeyko, A.Y., Zamora, N., 2016. Probabilistic tsunami hazard assessment for the Makran region with focus on maximum magnitude
771 assumption. Natural Hazards and Earth System Sciences 16, 1339–1350. doi:10.5194/nhess-16-1339-2016.

772 Kanamori, H., 1977. The energy release in great earthquakes. Journal of Geophysical Research (1896-1977) 82, 2981–2987. doi:10.1029/
773 JB082i020p02981.

774 Legrand, S., Deleersnijder, E., Hanert, E., Legat, V., Wolanski, E., 2006. High-resolution, unstructured meshes for hydrodynamic models of the
775 Great Barrier Reef, Australia. Estuarine, Coastal and Shelf Science 68, 36 – 46. doi:10.1016/j.ecss.2005.08.017.

776 Liu, X., Guillas, S., 2017. Dimension reduction for Gaussian process emulation: An application to the influence of bathymetry on tsunami heights.
777 SIAM/ASA Journal on Uncertainty Quantification 5, 787–812. doi:10.1137/16M1090648.

778 Lynett, P.J., 2016. Precise prediction of coastal and overland flow dynamics: A grand challenge or a fool's errand. Journal of Disaster Research 11,
779 615–623. doi:10.20965/jdr.2016.p0615.

780 Lynett, P.J., Borrero, J., Son, S., Wilson, R., Miller, K., 2014. Assessment of the tsunami-induced current hazard. Geophysical Research Letters
781 41, 2048–2055. doi:10.1002/2013GL058680.

782 Lynett, P.J., Borrero, J.C., Weiss, R., Son, S., Greer, D., Renteria, W., 2012. Observations and modeling of tsunami-induced currents in ports and
783 harbors. Earth and Planetary Science Letters 327-328, 68 – 74. doi:10.1016/j.epsl.2012.02.002.

784 Lynett, P.J., et al., 2017. Inter-model analysis of tsunami-induced coastal currents. Ocean Modelling 114, 14 – 32. doi:10.1016/j.ocemod.2017.
785 04.003.

786 Mathikolonis, T., Roeber, V., Guillas, S., 2019. Computationally efficient surrogate-based optimization of coastal storm waves heights and run-ups.
787 arXiv preprint arXiv:1910.01932 .

788 Ming, D., Guillas, S., 2019. Integrated emulators for systems of computer models. arXiv preprint arXiv:1912.09468 .

789 Moernaut, J., Daele, M.V., Fontijn, K., Heirman, K., Kempf, P., Pino, M., Valdebenito, G., Urrutia, R., Strasser, M., Batist, M.D., 2018. Larger
790 earthquakes recur more periodically: New insights in the megathrust earthquake cycle from lacustrine turbidite records in south-central Chile.
791 Earth and Planetary Science Letters 481, 9 – 19. doi:10.1016/j.epsl.2017.10.016.

792 Muhari, A., Charvet, I., Tsuyoshi, F., Suppasri, A., Imamura, F., 2015. Assessment of tsunami hazards in ports and their impact on marine vessels
793 derived from tsunami models and the observed damage data. Natural Hazards 78, 1309–1328. doi:10.1007/s11069-015-1772-0.

794 Okada, Y., 1985. Surface deformation due to shear and tensile faults in a half-space. Bulletin of the Seismological Society of America 75, 1135–1154.

795 Okal, E.A., Fritz, H.M., Raad, P.E., Synolakis, C., Al-Shijbi, Y., Al-Saifi, M., 2006. Oman field survey after the December 2004 Indian Ocean
796 tsunami. Earthquake Spectra 22, 203–218. doi:10.1193/1.2202647.

797 Park, H., Cox, D.T., 2016. Probabilistic assessment of near-field tsunami hazards: Inundation depth, velocity, momentum flux, arrival time, and
798 duration applied to Seaside, Oregon. Coastal Engineering 117, 79 – 96. doi:10.1016/j.coastaleng.2016.07.011.

799 Rashidi, A., Shomali, Z.H., Dutykh, D., Keshavarz Farajkhah, N., 2020. Tsunami hazard assessment in the Makran subduction zone. Natural
800 Hazards 100, 861–875. doi:10.1007/s11069-019-03848-1.

801 Reguly, I.Z., et al., 2018. The VOLNA-OP2 tsunami code (version 1.5). Geoscientific Model Development 11, 4621–4635. doi:10.5194/
802 gmd-11-4621-2018.

803 Salmanidou, D.M., Guillas, S., Georgiopoulou, A., Dias, F., 2017. Statistical emulation of landslide-induced tsunamis at the Rockall Bank, NE
804 Atlantic. Proceedings of the Royal Society A: Mathematical, Physical and Engineering Sciences 473, 20170026. doi:10.1098/rspa.2017.
805 0026.

806 Salmanidou, D.M., Heidarzadeh, M., Guillas, S., 2019. Probabilistic landslide-generated tsunamis in the Indus Canyon, NW Indian Ocean, using

statistical emulation. Pure and Applied Geophysics 176, 3099–3114. doi:10.1007/s00024-019-02187-3.

Scala, A., Lorito, S., Romano, F., Murphy, S., Selva, J., Basili, R., Babeyko, A., Herrero, A., Hoechner, A., Løvholt, F., Maesano, F.E., Perfetti, P., Tiberti, M.M., Tonini, R., Volpe, M., Davies, G., Festa, G., Power, W., Piatanesi, A., Cirella, A., 2019. Effect of shallow slip amplification uncertainty on probabilistic tsunami hazard analysis in subduction zones: Use of long-term balanced stochastic slip models. Pure and Applied Geophysics doi:10.1007/s00024-019-02260-x.

van Scheltinga, A.D.T., Myers, P.G., Pietrzak, J.D., 2012. Mesh generation in archipelagos. Ocean Dynamics 62, 1217–1228. doi:10.1007/s10236-012-0559-z.

Smith, G.L., McNeill, L.C., Wang, K., He, J., Henstock, T.J., 2013. Thermal structure and megathrust seismogenic potential of the makran subduction zone. Geophysical Research Letters 40, 1528–1533. doi:10.1002/grl.50374.

Straume, E.O., et al., 2019. Globsed: Updated total sediment thickness in the world's oceans. Geochemistry, Geophysics, Geosystems 20, 1756–1772. doi:10.1029/2018GC008115.

Ulrich, T., Vater, S. Madden, E.H., Behrens, J., van Dinther, Y., van Zelst, I., Fielding, E.J., Liang, C., Gabriel, A.A., 2019. Coupled, physics-based modeling reveals earthquake displacements are critical to the 2018 Palu, Sulawesi Tsunami. Pure and Applied Geophysics 176, 4069–4109. doi:10.1007/s00024-019-02290-5.